PHYSICAL REVIEW B **95**, 075426 (2017)

Correlation effects and quantum oscillations in topological nodal-loop semimetals

Jianpeng Liu and Leon Balents
Kavli Institute for Theoretical Physics, University of California, Santa Barbara, California 93106, USA

(Received 18 September 2016; revised manuscript received 24 January 2017; published 22 February 2017)

We study the unique physical properties of topological nodal-loop semimetals protected by the coexistence of time-reversal and inversion symmetries with negligible spin-orbit coupling. We argue that strong correlation effects occur at the surface of such systems for relatively small Hubbard interaction U, due to the narrow bandwidth of the "drumhead" surface states. In the Hartree-Fock approximation, at small U we obtain a surface ferromagnetic phase through a continuous quantum phase transition characterized by the surface-mode divergence of the spin susceptibility, while the bulk states remain very robust against local interactions and remain nonordered. At slightly increased interaction strength, the system quickly changes from a surface ferromagnetic phase to a surface charge-ordered phase through a first-order transition. When Rashba-type spin-orbit coupling is applied to the surface states, a canted ferromagnetic phase occurs at the surface for intermediate values of U. The quantum critical behavior of the surface ferromagnetic transition is nontrivial in the sense that the surface spin order parameter couples to Fermi-surface excitations from both surface and bulk states. This leads to unconventional Landau damping and consequently a naïve dynamical critical exponent $z \approx 1$ when the Fermi level is close to the bulk nodal energy. We also show that, already without interactions, quantum oscillations arise due to bulk states, despite the absence of a Fermi surface when the chemical potential is tuned to the energy of the nodal loop. The bulk magnetic susceptibility diverges logarithmically whenever the nodal loop exactly overlaps with a quantized magnetic orbit in the bulk Brillouin zone. These correlation and transport phenomena are unique signatures of nodal-loop states.

DOI: 10.1103/PhysRevB.95.075426

I. INTRODUCTION

The theoretical proposal and experimental verification of Weyl and Dirac semimetals [1–18] has shown that topological electronic structure is not restricted to gapped systems [19–23], but also occurs in gapless systems such as nodal metals [24]. Recently, the interest in topological semimetals has been extended from systems with point nodes to those with a three-dimensional (3D) nodal loop, "nodal chain" [25], "nodal arc"[26], and even "nodal surfaces" [27], in which there are bulk band touchings along isolated or connected 1D lines, or even at 2D surfaces in the 3D Brillouin zone (BZ) instead of at isolated points.

A growing number of material systems have been theoretically proposed to realize nodal-loop semimetals (NLSMs) [28–37]. In particular, ZrSiS and $\mathrm{PbTaSe_2}$ have been experimentally confirmed by angle-resolved photoemission spectroscopy (ARPES) measurements [31,32,34], and the bulk nodal loops in the ZrSiS-family compounds were further investigated by de Haas–van Alphen (dHvA) quantum oscillations [38,39] and magnetotransport measurements [40].

In this paper, we discuss some fundamental physics of NLSMs which is distinct from Weyl and Dirac systems. First, we argue that nodal-loop semimetals are prime candidates to observe correlation effects at their surfaces. This is because, unlike point node materials which possess highly dispersive bulk and surface states (typically with large Fermi velocities derived naturally from the several eV width of the associated bands), nodal-loop semimetals possess "drumheadlike" surface states. Depending on surface terminations, the states exist either inside or outside the projection of the nodal loop in the surface BZ.

The dispersion of such drumhead surface states is typically much smaller than that of the bulk valence and conduction bands, raising the interesting possibility of correlation effects occurring at the surface even when interactions are too weak to disturb the electronic states with large kinetic energy in the interior of the sample. Correlations may be induced by Coulomb interactions and/or coupling to phonons, due to the small kinetic energy and large surface density of states. For example, it has been theoretically proposed that such flat surface states might support s-wave superconductivity whose critical temperature scales linearly with the coupling strength [41–43]. Here we argue that repulsive Coulomb interactions generate unusual surface charge density wave and ferromagnetic states, for moderate interaction strength for which the bulk states are unaffected. We expound this in detail through a thorough Hartree-Fock study of a NLSM, including both Hubbard U and surface Rashba-like spin-orbit coupling (SOC) [44]. This yields a phase diagram showing several correlated surface phases at relatively small values of U.

Given the prospect for surface quantum phase transitions (QPTs) in these systems, it is interesting to explore the associated quantum critical behavior. We find that such *surface* QPTs can realize entirely different critical universality classes, different from either two- or three-dimensional bulk QPTs, owing to their mixed dimensional character. Specifically, a distinct process of Landau damping of order-parameter fluctuations into the third dimension arises, and dominates under conditions which we explain.

It is also important to be able to characterize a NLSM by probes other than photoemission, which may be difficult or impossible on many samples, or on appropriate crystal surfaces. In that vein, we derive the existence of unconventional quantum oscillations in NLSMs, which are present even when the Fermi level is exactly at the degeneracy level, so that the system has no true Fermi surface.

These results are expounded in detail in the remainder of the paper, which is organized as follows. In Sec. II, we first a noninteracting tight-binding (TB) model on a tetragonal lattice with both inversion ($\mathcal{P}$) and time-reversal ($\mathcal{T}$) symmetries, which can realize the NLSM phase when spin-orbit coupling (SOC) is neglected. Then, in Sec. III we apply on-site Hubbard interactions (the strength of the interaction is denoted by U), and solve such an interacting model in a slab geometry within the Hartree-Fock (HF) approximation, both with and without Rashba SOC, and complement the HF analysis with a study of the susceptibility in the random-phase approximation. Next, in Sec. IV, we consider Landau damping of ferromagnetic surface fluctuations, which control quantum critical phenomena [45,46]. We find in particular that when the Fermi level is close to the nodal energy, the dominant process is one in which an electron-hole pair is *shared* between the bulk and surface, leading to an unconventional dynamical coefficient $\sim |\nu_m| q_\parallel$ (ν_m is the bosonic Matsubara frequency, $q_\parallel$ is the magnitude of in-plane wave vector). This implies a different universality class for the ferromagnetic QPT. Finally, In Sec. V, we discuss quantum oscillations due to the bulk nodal-loop states, showing that they arise even in the absence of a Fermi surface, and conclude with a summary in Sec. VI.

II. NONINTERACTING TIGHT-BINDING MODEL

We first construct a noninteracting TB model on a tetragonal lattice with both $\mathcal{T}$ and $\mathcal{P}$ symmetries neglecting SOC. As schematically shown in Fig. 1(a), there are two sublattices denoted by A and B in each primitive cell, and the hopping from A to B along the positive (negative) z direction is denoted by t_1 (t_2). Moreover, there are intrasublattice in-plane hopping t_0 and intersublattice in-plane hopping t_3. Without the in-plane hoppings, the system can be considered as arrays of decoupled 1D Su-Schrieffer-Heeger (SSH) chains [47,48]; the in-plane hopping t_3 couple these chains together so that there is band inversion around only one of the eight time-reversal invariant momenta (TRIM). The nodal loop is centered around the TRIM with inverted band order.

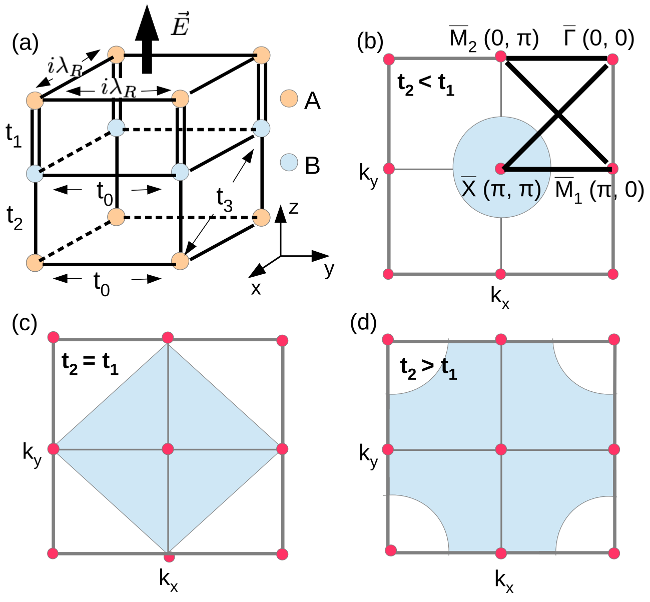

FIG. 1. Schematic illustration of the noninteracting tight-binding model for nodal-loop semimetals on a tetragonal lattice. (a) Lattice structure and hopping terms; the thick black arrow indicate surface electric field which generates Rashba SOC denoted by λ_R. (b)–(d) Nodal loops projected onto the (001) surface BZ, with the shaded region indicating the drumhead surface states, (b) for $t_2 < t_1$, (c) $t_2 = t_1$, and (d) $t_2 > t_1$.

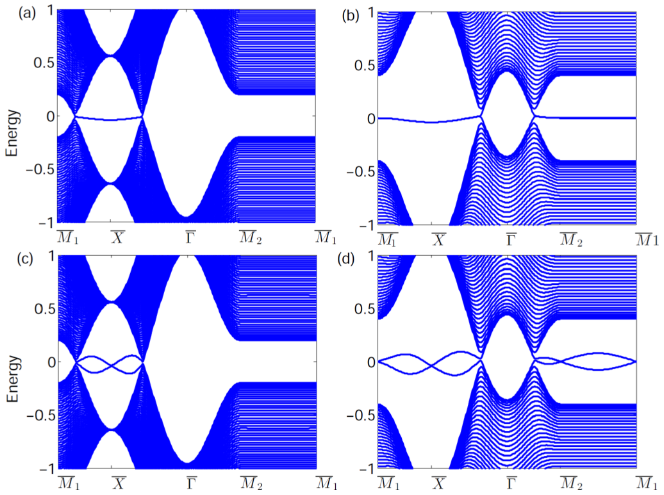

FIG. 2. Surface band structures of the noninteracting tight-binding model without surface SOC, (a) and (b), and with surface SOC, (c) and (d). (a) $t_2 = 0.75t_1$, and (b) $t_2 = 1.25t_1$; (c) $t_2 = 0.75t_1$, $\lambda_R = 0.0625t_1$, and (d) $t_2 = 1.25t_1$, $\lambda_R = 0.0625t_1$. The energy bands are plotted along the high-symmetry path marked by the thick black lines in Fig. 1(b).

Note that this model, defined on a bipartite lattice, possesses a "chiral symmetry" when $t_0 = 0$. In this special case, $\mathcal{C}H(\mathbf{k})\mathcal{C}^{-1} = -H(\mathbf{k})$, where $\mathcal{C} = \sigma_z$, and $H(\mathbf{k})$ is the model Hamiltonian at wave vector $\mathbf{k}$. This implies that if $E(\mathbf{k})$ is an eigenenergy at $\mathbf{k}$, then $-E(\mathbf{k})$ is also the eigenenergy. Adding the t_0 hopping term break this symmetry.

The specific properties of the nodal loop such as its size and shape are controlled by t_1, t_2, and t_3, while t_0 renders dispersions to both the bulk nodal energy along the loop and the otherwise flat drumhead surface states. Hereafter we fix $t_1 = 0.8$, $t_3 = 0.2$, $t_0 = 0.01$, and $t_2 > 0$ is the only variable in the noninteracting situation. In particular, when $t_2 < t_1$, there is a circular nodal loop centered at the X $[(\pi,\pi,\pi)]$ point. If the surface [49] is truncated at the A sublattice, one obtains drumhead surface states inside the projected nodal loop centered at $\overline{X}$ as shown in Figs. 1(b) and 2(a). If $t_2 = t_1$, the nodal loop is diamondlike and connects the TRIM X and M $[(\pi,0,\pi)]$. The corresponding surface states fill the region inside the diamond as shown in Fig. 1(c) [50]. When $t_2 > t_1$, the nodal loop is centered at Z $[(0,0,\pi)]$ and the surface states fill the region outside the projected nodal loop [Figs. 1(d) and 2(b)]. It worthwhile to note that for fixed bulk hopping parameters the drumhead surface states can be either inside or outside the projected nodal loop depending on surface terminations (see Appendix C), which is essentially due to the properties of 1D SSH chains. Therefore, the surface states covering a large portion of the surface BZ as shown in Fig. 1(d) can also be realized when $t_1 < t_2$ if the system is terminated at the other sublattice.

Given that inversion symmetry is always broken at a surface, the surface electric field may lead to considerable Rashba spin-orbit splittings in the surface states. Such surface Rashba splittings have been observed in the surfaces of nonmagnetic and magnetic metals [51–53], as well as semiconductor heterostructures [54]. Thus we also take the surface Rashba effects into account by adding a Rashba-type first-neighbor spin-dependent hopping within the surface atomic layer, of which the amplitude is denoted by λ_R. The spin-degenerate drumhead surface states are splitted by such surface SOC [see Figs. 2(c) and 2(d)]; moreover, the surface states acquire nontrivial spin textures. We thus expect that the effects of Coulomb interactions in these two situations (with and without surface SOC) would be different.

III. EFFECTS OF HUBBARD INTERACTIONS

A. Without surface Rashba spin-orbit coupling

We first consider the situation without surface Rashba splittings, and apply Hubbard interactions, $H_U = U\sum_i \hat{n}_{i\uparrow}\hat{n}_{i\downarrow}$, to the above noninteracting tight-binding model in a slab geometry. As the Coulomb interaction at the surface is expected to be strongly screened due to the large surface density of states (DOS), a Hubbard-type local interaction is a good description if we are mainly interested in the effects on the surface states. On the other hand, unlike the surface states of topological insulators, there is no simple low-energy effective Hamiltonian describing the drumhead surface states of NLSMs. Thus we have to construct a slab and apply Hubbard interactions to all the electrons in the slab. Hereafter we will only consider half-filled systems, and we say the system is charge homogeneous with zero charge density if each site is exactly half filled, i.e., there is one electron at each site.

The Hubbard interactions are treated by self-consistent Hartree-Fock (HF) approximation (see Appendix A for details). The HF ground states for a slab of 50 primitive cells are shown in Fig. 3(a). When $U = 0$, the system is in the NLSM phase. When $U \sim$ 10–20% t_1, the system enters into a surface FM (denoted by "surf FM" in the figure) phase with the ferromagnetic order localized at the surface. As U is further increased, a surface charge-ordered phase becomes energetically favored over the surface FM phase. The system enters into the surface CDW phase through a first-order transition. The inset in Fig. 3(a) shows the local charge density along the z direction for $U = 0.5t_1$ and $t_2 = 1.25t_1$. Clearly the charges are strongly localized at the surface, as the density oscillation decays rapidly into the bulk.

The smallness of the critical U for the instability of the NLSM surface states, demonstrated in the figure, is expected from the flatness of the surface band. More specifically, we would expect from the Stoner criteria of ferromagnetism that the critical U should be of order of the inverse density of states at the Fermi level, i.e., proportional to the surface stand bandwidth, or $4t_0$. Since $t_0 = 0.01$, the critical U may actually appear surprisingly *large*. This is due to the fact that the surface states have a nonzero width, and so the effective interaction is reduced by the wave-function amplitude at the surface.

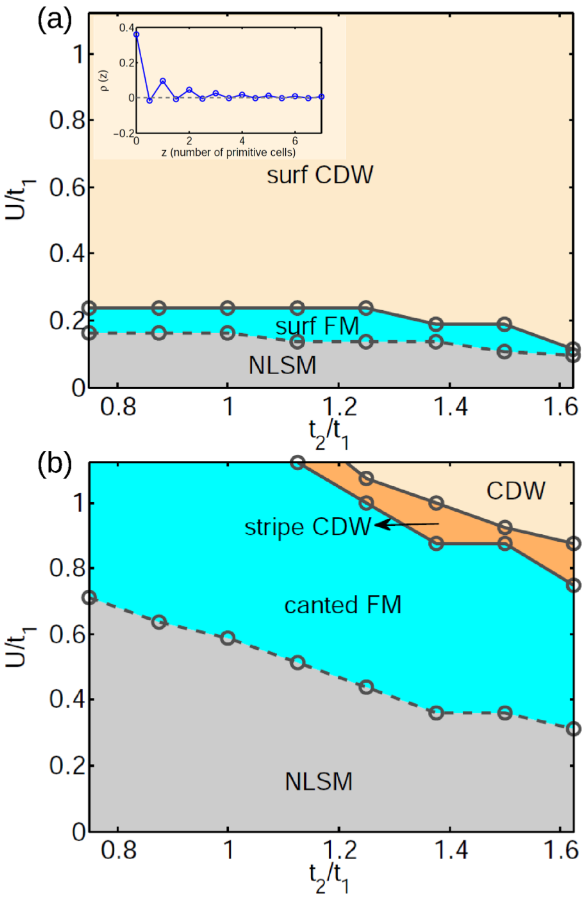

FIG. 3. Phase diagram of the NLSMs with Hubbard interactions in the $t_2 - U$ parameter space: (a) without surface Rashba SOC, with the inset shows the local charge density distribution in the surface CDW phase when $t_2 = 1.25t_1$ and $U = 0.5t_1$, and (b) with surface Rashba SOC, where $\lambda_R = 0.0625t_0$.

To study the nature of the surface FM transition, we have calculated the spin susceptibility of a 30-primitive-cell slab in the random-phase approximation (RPA) [55] (see Appendix B for details). Fig. 4(a) shows the eigenvalues of static RPA spin susceptibility at different wave vectors at $U = 0.25t_1$ and $t_2 = t_1$. As clearly shown in the figure, there are a large number of quasidegenerate bands with small amplitudes; moreover, there are two degenerate bands with much larger amplitudes which tend to diverge at Γ. The eigenvectors of the RPA spin susceptibility indicate that those quasidegenerate bands with small amplitudes are from the bulk spin fluctuations, while the two bands with much larger amplitudes are dominated by acoustic and optical surface fluctuation modes. This is consistent with the expectation that the drumhead surface states are much more sensitive to Coulomb interactions than the bulk states due to the much smaller bandwidth. From Fig. 4(a) it is also evident that the surface spin-fluctuation modes tend to diverge at $\overline{\Gamma} = (0,0)$, indicating a continuous quantum phase transition at the surface driven by Hubbard interactions. We refer the readers to Appendix B for technical details of the implementation of RPA on the slab as well as the properties of the eigenvalues and the eigenvectors of the spin susceptibility.

In Fig. 4(b) we show the parameter dependence of the RPA surface spin susceptibility at $\overline{\Gamma} = (0,0)$ calculated in a slab geometry including 30 primitive cells, which is denoted

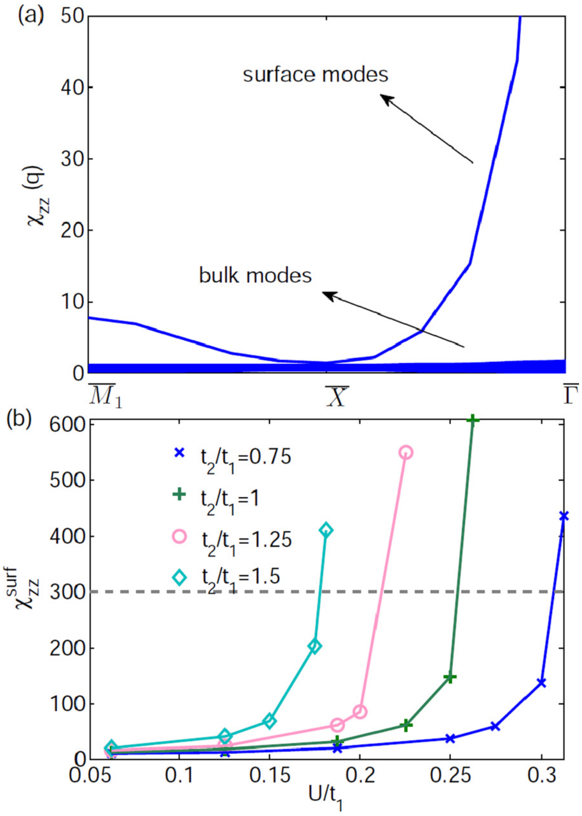

FIG. 4. (a) Dispersion of the spin susceptibility ($\chi_{zz}(q)$) for a 60-layer slab of nodal-loop metal with $t_2 = t_1$ and $U = 0.25t_1$. (b) The U dependence of the surface spin fluctuations at Γ (denoted by $\chi^{\rm surf}_{zz}$) for different t_2 values.

by $\chi^{\rm surf}_{zz}(\Gamma)$. As is clearly seen from the figure, for a given t_2, the surface fluctuation modes at $\overline{\Gamma}$ increase with U, and diverge at some critical U, indicating the transition from a nonordered phase to a surface FM phase. The gray dotted line in Fig. 3(b) marks the numeric threshold above which $\chi^{\rm surf}_{zz}(\Gamma)$ is considered as diverging. It is interesting to note that as t_2 increases from $0.75t_1$ (denoted by blue crosses) to $1.5t_1$ (denoted by cyan diamonds), the critical U value is reduced by $\sim$50%. This is because the surface DOS becomes larger for greater t_2 values [Figs. 1(b)–1(d)], thus the system becomes more sensitive to Coulomb interactions [56].

B. Hubbard interactions with surface Rashba SOC

We continue to study the effects of Hubbard interactions on NLSMs including surface Rashba splittings with $\lambda_{\rm R} = 0.0625t_1$. Since the surface electric field decays quickly into the bulk, it is assumed that the Rashba SOC $\lambda_{\rm R}$ applies only to the topmost and bottommost layers of the slab. The system with such surface SOC expects to be more robust against Coulomb interactions due to the lifted spin degeneracy of the drumhead surface states as shown in Figs. 2(c)–2(d). Moreover, as the surface states at the Fermi level acquire nontrivial spin textures due to Rashba SOC, it is unlikely that a charge-ordered phase would be favored.

Both of the above two conjectures are numerically verified as shown in Fig. 3(b). When surface SOC is turned on, our noncollinear self-consistent HF calculations (see Appendix A for technical details) suggest that the system tends to enter into a surface canted FM phase around some moderate U values ($U_{\rm c} \sim 35$–$65\%\, t_1$). The surface canted FM phase is characterized by ferromagnetically coupled z components of spins (m_z) which are exponentially localized at the surface, and possibly with small spin cantings toward the in-plane directions.

We have also checked the U dependence of m_z at the surface layer, and find that $|m_z|$ increases continuously with U when $U \geqslant U_c$, indicating a continuous quantum phase transition. The critical value U_c decreases with the increase of t_2 due to the larger surface DOS for greater t_2 values. The continuous quantum phase transition is further verified by the divergence of surface spin susceptibility (data not shown). Moreover, it turns out that $|m_z|$ is likely to have a square-root dependence on $U - U_c$ ($|m_z| \sim \sqrt{U - U_c}$), which is in agreement with the behavior of Stoner ferromagnetism [57].

The spin susceptibilities are expected to be anisotropic due to the surface Rashba SOC, thus the in-plane spin susceptibilities χ_{xx} and χ_{yy} deserve further discussions. The RPA surface in-plane spin susceptibilities [denoted by $\chi^{\rm surf}_{xx}(\mathbf{q})$ and $\chi^{\rm surf}_{yy}(\mathbf{q})$] are shown in Fig. 5. The blue circles, magenta crosses, red diamonds, and cyan plus signs represent the cases of $t_2 = 0.75t_1, t_2 = t_1, t_2 = 1.25t_1$, and $t_2 = 1.5t_1$ respectively; the U value is fixed as $0.5t_1$. As shown from the figure,

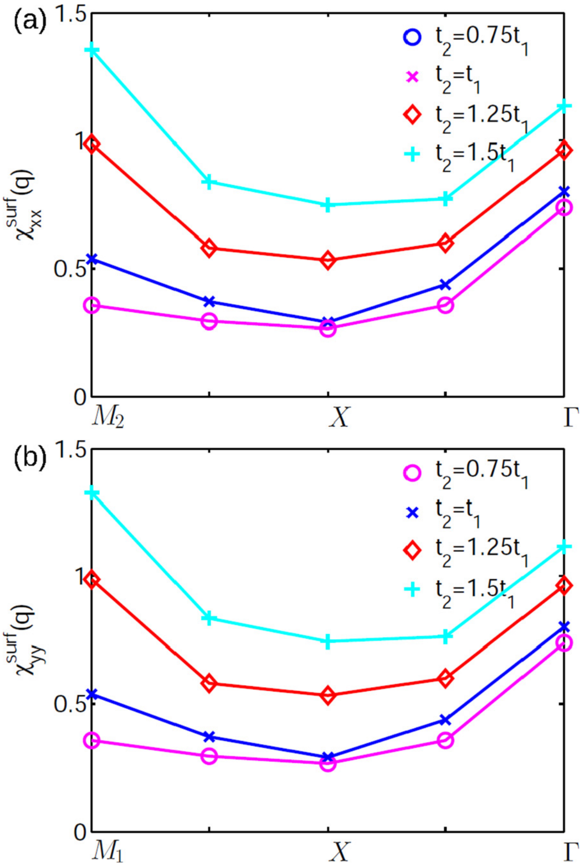

FIG. 5. Wavevector dependence of the surface-mode in-plane spin susceptibilities for different t_2 values at fixed $U = 0.5t_1$, (a) χ_{xx}, and (b) χ_{yy}. The high-symmetry points $M_1 = (\pi,0)$, $M_2 = (0,\pi)$, $X = (\pi,\pi)$, and $\Gamma = (0,0)$.

when $t_2 \lesssim 1.25t_1$, both $\chi^{\text{surf}}_{xx}(\mathbf{q})$ and $\chi^{\text{surf}}_{yy}(\mathbf{q})$ are peaked at Γ, indicating that the in-plane spin fluctuations tend to preserve the lattice translational symmetry. While when $t_2 \gtrsim t_1$, the peak of $\chi^{\text{surf}}_{xx}(\mathbf{q})$ is shifted to $M_2 = (0,\pi)$, and correspondingly $\chi^{\text{surf}}_{yy}(\mathbf{q})$ becomes peaked at $M_1 = (\pi,0)$. It implies that the in-plane spin components might develop some interesting winding textures in such a way that the x component (y component) is ordered antiferromagnetically along the y (x) direction. More details of computing the surface RPA spin susceptibilities are shown in Appendix B.

More interestingly, when $t_2 > t_1$ the system tends to go to a surface stripe charge-ordered phase [indicated by "stripe CDW" in Fig. 3(b)] at large U values, in which there are alternating positive and negative charge stripes along either the x or the y direction at the surface. There is a transition from such a surface stripe CDW phase to a surface CDW with homogeneous in-plane charge density as U further increases. Both of these transitions (from canted FM to stripe CDW phase, and from stripe CDW to in-plane homogeneous CDW phase) turn out to be first-order transitions whose phase boundaries are marked by solid lines as shown in Fig. 3(b). Again, we emphasize that the charge and spin order parameters in all of these phases are exponentially localized at the surface and the bulk remains nonordered.

In concluding this section, we remark that the mean-field treatment is of course approximate, and so that some quantitative differences from exact results should be expected. This may be exacerbated by the gapless bulk quasiparticle states, which remain gapless even in the ordered phases [58]. However, we believe the mean-field results should be qualitatively correct, and that the results capture the proper variation with coupling constants, etc. To go beyond this approach, it would be interesting for the surfaces of nodal-loop metals using more advanced many-body numerical techniques such as quantum Monte Carlo or dynamical mean field theory. However, this is certainly beyond of the scope of the present paper, and we leave it for future study.

IV. FERROMAGNETIC QUANTUM CRITICALITY AT THE SURFACE

A. Framework and general considerations

In this section we discuss the quantum critical (QC) behavior near the ferromagnetic transition at the surface of a nodal-loop semimetal neglecting effects of surface SOC. The prototypical description of the quantum phase transition in an itinerant ferromagnet is that of Hertz-Millis theory [45,46], in which the system is described by an effective action for the order parameter in which the itinerancy of the electrons is reflected by a term representing Landau damping, due to the coupling with Fermi-surface fluctuations [59]. The Landau damping gives rise to a term quadratic in the order parameter with a dynamical coefficient $\sim|\nu_m|/q$ in the effective action of the spins. Based on this, Hertz derived the dynamical critical exponent $z = 3$ for FM transitions in 2D and 3D Fermi-liquid systems [45]. The dynamical critical exponent determines the quantum critical phenomenology such as the dependence of critical temperatures on U, the specific heat, and the crossover behavior from quantum to classical regime at finite temperatures [45,46]. In two dimensions, there are known flaws in the purely order parameter description, and much theoretical work has gone into improving it [60–62]. Nevertheless, the dynamical scaling $z \approx 3$ is believed to still be quite a good approximation, if not exact.

In NLSMs, we have shown in Sec. III that the FM transition occurs only at the surface and no order occurs in the bulk, so that one may naïvely expect purely two-dimensional FM quantum criticality with $z \approx 3$. However, in reality the situation is more complicated due to the gapless bulk states. The electron-hole excitations which couple to the surface spin order parameter arise both from the surface bound states and the extended bulk states, which have an amplitude at the surface. Given the critical role of Landau damping in the theory, we may expect that the quantum critical behavior would be different for such a surface FM transition with gapless bulk excitations.

We confine our analysis here to the level of Landau damping, i.e., the Hertz-Millis order-parameter description, which is sufficient to distinguish the difference between purely 2D critical behavior and something else. This is already somewhat subtle because several distinct processes may contribute to the damping, i.e., the nonanalytic part of the surface spin susceptibility, and one must carefully take into account the momentum and frequency behavior of surface Green's functions in describing this. It is convenient to decompose the electron-hole excitations into different types. In the first type, both the electron and the hole are created in the surface bound states as denoted by "$s - s$" in Fig. 6(a), in the second type, that both the electron and the hole are created in the bulk continuum which is denoted as "$b - b$" in Fig. 6, and finally in the last type, a hole is created in the surface states while an electron is added to the bulk states as denoted by "$s - b$" in Fig. 6(b).

We consider two different situations. The first situation is that the system is (slightly) hole-doped with partially filled surface bands as schematically shown in Fig. 6(a). In the second situation, the Fermi level is very close to the nodal energy and the drumhead surface states are almost completely filled as sketched in Fig. 6(b). In the first situation we only consider the $s - s$ and $b - b$ type excitations, since the $s - b$ process requires a large momentum transfer, and we are only interested in low-frequency long-wavelength excitations; while in the second case we only consider the $s - b$ and $b - b$ excitations since the surface bands are fully occupied.

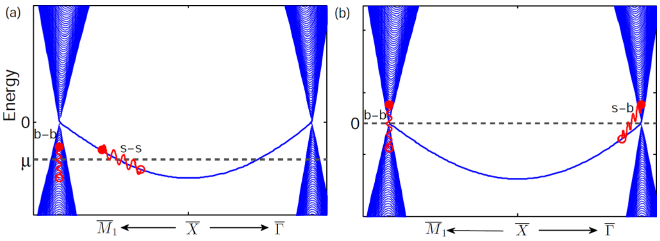

FIG. 6. Schematic illustration of different types of electron-hole excitations that couple to surface spins. (a) When the surface bands are partially filled. (b) When the surface bands are (nearly) completely filled. The electron-hole excitations purely from the surface (bulk) states are denoted by "*s*-*s*" ("*b*-*b*"), while the process of creating a hole in the surface states and an electron in the bulk states is denoted by "*s*-*b*."

B. Surface Green's function and dynamical susceptibility

We start by calculating the surface Green's function (SGF) of NLSMs using the method reported in Ref. [63]. Note that the SGF includes contributions from both extended and localized eigenstates, and by using an exact method for calculating the SGF, we capture subtle behaviors due to varying contributions of the two types of states. For the tight-binding model given in Sec. II, the surface Green's function $[G_s(\mathbf{k}_\parallel,\omega)]$ can be calculated analytically at low energies when the size of the nodal loop is much smaller than that of the BZ. It turns out that the SGF has a simple analytic solution,

$$G_s(\mathbf{k}_\parallel,\omega) = \frac{-\widetilde{\omega}}{\widetilde{t}_1[(\sqrt{\gamma^2-4}+\gamma)/2 - t_2/\widetilde{t}_1]} \approx -\frac{1}{t_2}\frac{\widetilde{\omega}}{\sqrt{\left(k_\parallel^2-k_0^2\right)^2-\widetilde{\omega}^2}+k_\parallel^2-k_0^2}, \tag{1}$$

where $\mathbf{k}_\parallel = (k_x,k_y)$, $\gamma = (\widetilde{t}_1^2 + t_2^2 - t_2^2\widetilde{\omega}^2)/(\widetilde{t}_1 t_2)$, and

$$\begin{aligned}\widetilde{\omega} &= [\omega - 2t_0(\cos k_x + \cos k_y) + \widetilde{\mu}]/t_2,\\ &\approx \left\{\omega - \left[t_0\left(k_x^2+k_y^2\right) - 4t_0\right] + \widetilde{\mu}\right\}/t_2,\end{aligned} \tag{2}$$

where $\widetilde{\mu} = \mu/t_2$ with μ being the Fermi level, and

$$\begin{aligned}\widetilde{t}_1 &= t_1 + 2t_3(\cos k_x + \cos k_y)\\ &\approx t_1 - 4t_2 + t_2\left(k_x^2+k_y^2\right).\end{aligned} \tag{3}$$

We consider the situation that the nodal loop is centered at (π,π,π), the radius of which is much smaller than the size of the Brillouin zone, and assume that $t_2 = t_3$, which is nothing but saying that the bulk Fermi velocity is isotropic [64]. Then the second lines in Eqs. (2) and (3) follow by expanding $\cos k_x$ and $\cos k_y$ around $k_x = \pi$ and $k_y = \pi$. In Eq. (1) k_0 is introduced as a parameter characterizing the size of the nodal loop:

$$\widetilde{t}_1 - t_2 = t_3\left(k_\parallel^2 - k_0^2\right) = t_2\left(k_\parallel^2 - k_0^2\right). \tag{4}$$

Again, we have assumed that $t_2 = t_3$ so that the bulk Fermi velocity is isotropic. Starting from Eq. (1) it is straightforward to show that when $-|k_\parallel^2 - k_0^2| \leqslant \widetilde{\omega} \leqslant |k_\parallel^2 - k_0^2|$, ω is in the bulk gap (the gap is locally defined at each $\mathbf{k}$ and vanishes at the nodal loop), and there is a pole at $\widetilde{\omega} = 0$ for $k_\parallel < k_0$ corresponding to the drumhead surface states (the surface is prepared by making a truncation at the A sublattice), while when $\widetilde{\omega} > |k_\parallel^2 - k_0^2|$ or $\widetilde{\omega} < |k_\parallel^2 - k_0^2|$, ω is in the bulk continuum. Hereafter we will set the bulk nodal energy as 0, so $\widetilde{\omega}$ is shifted by a small constant: $t_2\widetilde{\omega} = \omega - t_0(k_\parallel^2 - k_0^2) + \widetilde{\mu}$. We refer the readers to Appendix C for details in calculating the surface Green's function.

Equation (1) may be expressed using the spectral representation as

$$G_s(\mathbf{k}_\parallel,\omega) = \frac{1}{t_2}\int d\epsilon\, \frac{f(\mathbf{k}_\parallel,\epsilon)}{\omega/t_2 - (\epsilon - \widetilde{\mu}) + i\delta_\epsilon}, \tag{5}$$

where δ_ϵ is an infinitesimal quantity which is greater than (less than) zero if $\epsilon > \widetilde{\mu}$ ($\epsilon < \widetilde{\mu}$). Or, in the Matsubara formalism,

$$G_s(\mathbf{k}_\parallel,i\omega_n) = \frac{1}{t_2}\int d\epsilon\, \frac{f(\mathbf{k}_\parallel,\epsilon)}{i\omega_n/t_2 - (\epsilon - \widetilde{\mu})}, \tag{6}$$

The spectral density $f(\mathbf{k}_\parallel,\epsilon)$ consists of two terms:

$$f(\mathbf{k}_\parallel,\epsilon) = f_b(\mathbf{k}_\parallel,\epsilon) + f_s(\mathbf{k}_\parallel,\epsilon). \tag{7}$$

$f_b(\mathbf{k}_\parallel,\epsilon)$ is from the bulk continuum, and $f_s(\mathbf{k}_\parallel,\epsilon)$ corresponds to the surface bound state:

$$\begin{aligned}f_b(\mathbf{k}_\parallel,\epsilon) &= \frac{\sqrt{(\epsilon - \widetilde{t}_0 x_{k_\parallel})^2 - x_{k_\parallel}^2}}{\epsilon - \widetilde{t}_0 x_{k_\parallel}}\theta(|\epsilon - \widetilde{t}_0 x_{k_\parallel}| - |x_{k_\parallel}|),\\ f_s(\mathbf{k}_\parallel,\epsilon) &= |x_{k_\parallel}|\delta(\epsilon - \widetilde{t}_0 x_{k_\parallel})\theta(-x_{k_\parallel}),\end{aligned} \tag{8}$$

where $x_{k_\parallel} = k_\parallel^2 - k_0^2$, and $\widetilde{t}_0 = t_0/t_2$.

Now it is straightforward to calculate the dynamical susceptibility using the surface Green's function shown in Eq. (5)–(8). To be specific, using the Matsubara formalism, the dynamical susceptibility is expressed as

$$\chi(\mathbf{q}_\parallel,i\nu_m) = -\frac{1}{\beta}\int_{\mathbf{k}_\parallel}\sum_n G_s(\mathbf{k}_\parallel,i\omega_n)G_s(\mathbf{k}_\parallel + \mathbf{q}_\parallel,i\omega_n + i\nu_m), \tag{9}$$

where $\int_{\mathbf{k}_\parallel} = \int dk_x dk_y/(2\pi)^2$, $\beta = 1/(k_{\mathrm{B}}T)$ is the inverse temperature, and ($\mathbf{k}$, ω) and ($\mathbf{q}$, ν) denote Fermionic and Bosonic wave vectors and frequencies respectively. $\mathbf{k}_\parallel$ ($\mathbf{q}_\parallel$) represents an in-plane wave vector. Plugging Eq. (5) in to Eq. (9), and summing over the Matsubara frequencies using the standard contour technique, then taking the analytic continuation $i\nu_m \to \nu + i\delta$, one obtains

$$\mathrm{Im}\,\chi(\mathbf{q}_\parallel,\nu,\mu) = \int_{\mathbf{k}_\parallel}\int_{-\widetilde{\mu}}^{-\widetilde{\mu}+\widetilde{\nu}}\frac{d\epsilon}{t_2}\, f(-\epsilon,\mathbf{k}_\parallel)f(\widetilde{\nu}-\epsilon,\mathbf{k}_\parallel + \mathbf{q}_\parallel), \tag{10}$$

where $\widetilde{\mu} = \mu/t_2$, and $\widetilde{\nu} = \nu/t_2$, with μ being the Fermi level. Since $f = f_s + f_b$, $\chi(\mathbf{q}_\parallel,\nu)$ can be decomposed into four terms which are the bulk-bulk (χ_{bb}), surface-bulk (χ_{sb}), bulk-surface (χ_{bs}), and surface-surface (χ_{ss}) contributions. We will discuss these contributions separately in the following paragraphs.

C. Partially filled surface bands

Let us first consider the situation with partially filled surface bands as shown in Fig. 6(a) with $\mu < 0$. The dynamical susceptibility contributed by the $s-s$ process [denoted by $\chi_{ss}(\mathbf{q}_\parallel,\nu)$] behaves similarly to the 2D Linhard function because the SGF has a pole at $\widetilde{\omega} = 0$ for $k_\parallel < k_0$, which looks similar to that of 2D free electrons with quadratic dispersion. Thus the imaginary part of zero-temperature susceptibility $\mathrm{Im}\chi_{ss}(\mathbf{q}_\parallel,\nu) \sim \nu/q_\parallel$ at small in-plane wave vector $q_\parallel$ and low frequency $\nu \ll \hbar v_{\mathrm{F}}^s q_\parallel$ with v_{F}^s referring to the Fermi velocity of the surface bands [in the finite-temperature formalism $\chi_{\mathrm{ss}}(\mathbf{q}_\parallel,\nu_m) \sim |\nu_m|/q_\parallel$ with ν_m being Bosonic Matsubara frequency]. On the other hand, the dynamical susceptibility contributed by the $b-b$ process $\chi_{\mathrm{bb}}(\mathbf{q}_\parallel,\nu)$ with $|\nu| < |\mu|$ is expressed as

$$\begin{aligned}&\mathrm{Im}\,\chi_{\mathrm{bb}}(\mathbf{q}_\parallel,\nu,\mu)\\ &\quad= \int_{\mathbf{k}_\parallel}\int_{-\widetilde{\mu}}^{-\widetilde{\mu}+\widetilde{\nu}}\frac{d\epsilon}{t_2}\, f_b(-\epsilon,\mathbf{k}_\parallel)f_b(\nu-\epsilon,\mathbf{k}_\parallel + \mathbf{q}_\parallel),\end{aligned} \tag{11}$$

After some algebra, it turns out that when $\nu \ll \hbar v_{\mathrm{F}} q_{\|}$ (v_{F} is the bulk Fermi velocity):

$$\operatorname{Im} \chi_{\mathrm{bb}}(\mathbf{q}_{\|},\nu,\mu) \sim \frac{\nu}{q_{\|}}. \tag{12}$$

Therefore χ_{bb} is equally important as χ_{ss} for the hole-doped case. In other words, the dominant Landau damping is from both the surface and the bulk, and they make comparable contributions. Thus we expect the usual theory of 2D FM quantum critical still applies, with consequently dynamical critical exponent $z \approx 3$. It is also interesting to note that as a result of the fluctuations in the third spatial dimension, $\chi_{bb}(\mathbf{q}_{\|},\nu)$ is nonvanishing even when $q_{\|} = 0$. It turns out that

$$\operatorname{Im}\chi_{bb}(q_{\|} = 0,\nu,\mu) \sim \nu, \tag{13}$$

which is unusual for a ferromagnetic phase transition. We refer the readers to Appendix D for the derivations of Eqs. (12) and (13).

The analytic results shown in Eqs. (11) and (13) are supported by direct numeric calculations of the surface dynamical susceptibility of a 500-cell slab of the tight-binding model introduced in Sec. II. The Fermi level $\mu = -0.036$ as schematically indicated by the gray dashed line in Fig. 6(a), $t_0 = 0.01$, $t_1 = 0.8$, $t_2 = 0.3$, and $t_3 = 0.2$. The frequency dependence of surface dynamical susceptibility at $q_{\|} = 0$ is shown in Fig. 7(a). Clearly at low frequencies, $\chi_{\mathrm{bb}}(0,\nu)$ is linear in ν, in agreement with Eq. (13).

We also study the wave-vector dependence of $\chi_{\mathrm{bb}}(\mathbf{q}_{\|},\nu)$ for a given frequency $\nu = 0.008$ as shown in Fig. 7(b). $\operatorname{Im} \chi_{\mathrm{bb}}(\mathbf{q}_{\|},\nu)$ is linearly dependent on $1/q_x$ for $0.065 \lesssim q_{\|} \lesssim 0.085$ (in units of $1/a$, where $a = 1$ is the in-plane lattice constant). When $q_{\|} \lesssim 0.06$, we are no longer in the regime that $\nu \ll \hbar v_{\mathrm{F}} q_{\|}$ and in the meanwhile $1/q_{\|}$ becomes comparable to the **k**-mesh density, so that Eq. (12) is no longer valid; while when $q_{\|}$ is large ($q_{\|} \gtrsim 0.085$), the wave vector becomes comparable to the radius of the bulk "Dirac cone" above which the electron-hole excitations are rigorously truncated. This explains why the $1/q_{\|}$ behavior is observed only for $0.065 \lesssim q_{\|} \lesssim 0.086$. The details of computing the surface dynamical susceptibility are explained in Appendix E.

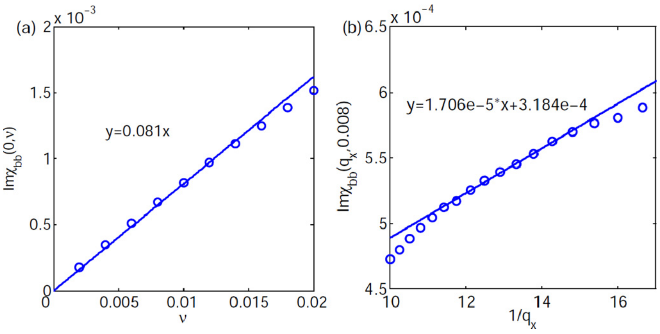

FIG. 7. Numerical calculations of the surface dynamical susceptibility of slightly hole-doped nodal-loop semimetals with partially filled surface bands: (a) frequency dependence at $q_{\|} = 0$; and (b) wave-vector dependence at $\nu = 0.008$. Note the horizontal axis in (b) is $1/q_x$.

D. Nearly full surface bands

We continue studying the case when the surface bands are nearly completely filled as shown in Fig. 6(b). In such a situation, the Fermi level $\mu = 0$, and the dominating contribution is either a $b-b$ or $s-b$ process. The surface dynamical susceptibility from the $s-b$ process is expressed as

$$\operatorname{Im} \chi_{\mathrm{sb}}(\mathbf{q}_{\|},\nu,\mu = 0) = \int_{\mathbf{k}_{\|}} \int_0^{\tilde{\nu}} \frac{d\epsilon}{t_2} f_s(-\epsilon,\mathbf{k}_{\|}) f_b(\nu - \epsilon,\mathbf{k}_{\|} + \mathbf{q}_{\|}), \tag{14}$$

and the $b-b$ contribution is expressed in Eq. (11) with $\mu = 0$. After solving these integrals, it turns out that

$$\operatorname{Im} \chi_{\mathrm{bb}}(\mathbf{q}_{\|},\nu,\mu = 0) \sim \nu^3/q_{\|}, \tag{15}$$

$$\operatorname{Im} \chi_{\mathrm{sb}}(\mathbf{q}_{\|},\nu,\mu = 0) \sim q_{\|}[\nu - \eta(t_0,q_{\|})], \tag{16}$$

where $\eta(t_0,q_{\|}) = 2t_0(2k_0 q_{\|} - q_{\|}^2)/3$ is the energy gap of the $s-b$ particle-hole excitations. Physically Eq. (16) implies that a minimal frequency $\sim\eta(t_0,q_{\|})$ is required to create an electron-hole pair of the $s-b$ type with finite wave vector $q_{\|}$. Such a minimal excitation energy $\sim t_0$, and vanishes when the surface bands are perfectly flat (remember that the surface bandwidth arises due to t_0) or when $q_{\|} \to 0$. We refer the readers to Appendix D for the derivations of Eqs. (15) and (16).

Equations (15) and (16) indicate that when $\mu = 0$ the $s-b$ process dominates over the $b-b$ process at low frequencies and small wave vectors. If we follow the Hertz-Millis procedure, a straightforward analysis then predicts the dynamical critical exponent $z \approx 1$. Subtleties similar to those in the purely 2D case may still occur here, of course, but this result is sufficient to show that the quantum critical behavior at this transition is fundamentally different from that of a purely 2D itinerant ferromagnet. We once again note that, when $q_{\|} = 0$, $\operatorname{Im} \chi_{bb}(0,\nu)$ is nonvanishing and $\sim\nu^2$ for $\mu = 0$ due to the Fermionic fluctuations in the z direction.

Again, the analytic results in Eqs. (15) and (16) are numerically verified by directly computing the surface-layer dynamical susceptibility of a 500-cell slab. The Fermi level is very close to the nodal loop in the calculations as indicated by the gray dashed line in Fig. 6(b). The surface bound states are almost completely filled. The other parameters of the tight-binding model are the same as those in the previous

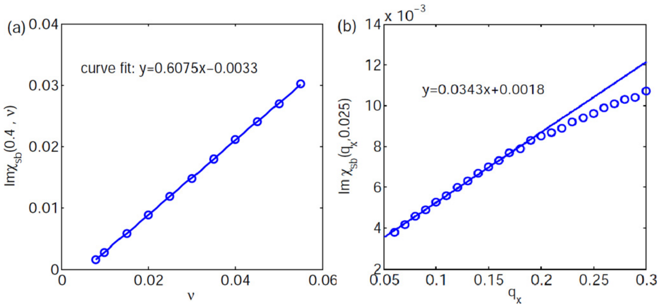

FIG. 8. Numerical calculations of the surface dynamical susceptibility of charge neutral nodal-loop semimetals with nearly completely filled surface bands: (a) the frequency dependence at $q_{\|} = 0.4$, and (b) the wave-vector dependence at $\nu = 0.025$.

TABLE I. Linear fits to the frequency dependence of surface susceptibility at different wave vectors.

$q_\parallel$	0.4	0.3	0.25	0.2	0.15	0.1	0.05
c	0.6075	0.5099	0.4536	0.3892	0.3143	0.2294	0.1377
$\eta(t_0,q_\parallel)$	0.0054	0.0041	0.0036	0.0030	0.0025	0.0017	0.0014

susceptibility calculation. The frequency dependence of the surface susceptibility at $q_\parallel = 0.4$ [denoted by $\mathrm{Im}\,\chi_{\mathrm{sb}}(0.4,\nu)$] is shown in Fig. 8(a). Clearly $\mathrm{Im}\,\chi_{\mathrm{sb}}(0.4,\nu) \sim \nu$ at low frequencies and there is a small energy gap around $\nu \sim t_0$, in agreement with Eq. (16).

In order to study the wave-vector dependence of the energy gap $\eta(t_0,q_\parallel)$, we have calculated the frequency dependence of the surface dynamical susceptibility of a 500-cell slab for different wave vectors from $q_\parallel = 0.4$ to $q_\parallel = 0.05$. Then we fit the data with linear functions $y = c\,[x - \eta(t_0,q_\parallel)]$ [y is $\mathrm{Im}\,\chi_{\mathrm{sb}}(q_\parallel,\nu)$, x is ν]. The parameters cs and $\eta(t_0,q_\parallel)$s are shown in Table I. As clearly shown in the table, $\eta(t_0,q_\parallel)$ decreases with $q_\parallel$ and tends to vanish as $q_\parallel \to 0$ [65].

We also numerically calculate the wave-vector dependence of the surface dynamical susceptibility at $\nu = 0.025$ as shown in Fig. 8(b). Clearly $\mathrm{Im}\,\chi_{\mathrm{sb}}(q_\parallel,0.025) \sim q_\parallel$ at small $q_\parallel$, in agreement with the analytic prediction of Eq. (16). It should be noted that when the Fermi level is at the nodal energy, the $b-b$ process is suppressed at relatively large wave vector ($q_\parallel \gtrsim 0.05$), thus the data shown in Figs. 8(a) and 8(b) are mostly contributed by a $s-b$ process. We refer the readers to Appendix E for details in the the numeric calculations of surface dynamical susceptibility.

V. BULK QUANTUM OSCILLATIONS

We turn to discussing the bulk quantum oscillations of NLSMs neglecting Coulomb interactions. We introduce the following low-energy effective Hamiltonians describing nodal loops with different in-plane dispersions:

$$\begin{aligned} H_0^{\mathrm{qua}} &= \hbar v_z k_z\,\sigma_y + \left(\Delta - \frac{\hbar^2\left(k_x^2+k_y^2\right)}{2m}\right)\sigma_z, \\ H_0^{\mathrm{lin}} &= \hbar v_z k_z\,\sigma_y + \left(\Delta - \hbar v_0\sqrt{k_x^2+k_y^2}\right)\sigma_z, \end{aligned} \tag{17}$$

where σ_y and σ_z are the Pauli matrices representing the lowest conduction band and highest valence band at some high-symmetry point [$\mathbf{k} = (0,0,0)$], v_z is the Fermi velocity along the z direction, and Δ is the gap at $\mathbf{k} = (0,0,0)$. H_0^{qua} describes a circular nodal loop with quadratic in-plane dispersion, of which the in-plane effective mass is denoted by m; while H_0^{lin} describes a nodal loop with linear in-plane dispersion with in-plane Fermi velocity v_0. The nodal energies described by Eq. (17) are exactly zeros.

The Landau levels for the above two effective Hamiltonians with $\mathbf{B} = B\hat{e}_z$ are readily obtained:

$$\begin{aligned} E_\pm^{\mathrm{qua}}(n,k_z) &= \pm\sqrt{(\Delta - \hbar\omega_c(n+1/2))^2 + \hbar v^2 k_z^2}, \\ E_\pm^{\mathrm{lin}}(n,k_z) &= \pm\sqrt{(\Delta - \hbar\omega_c\sqrt{n+1/2})^2 + \hbar v^2 k_z^2}, \end{aligned} \tag{18}$$

where the cyclotron frequency

$$\omega_c = \begin{cases} eB/m & \text{for quadratic in-plane dispersion} \\ \sqrt{2eBv_0^2/\hbar} & \text{for linear in-plane dispersion} \end{cases} \tag{19}$$

for the case of linear dispersion. If the chemical potential is exactly at the nodal energy, i.e., $\mu = 0$, in general the Landau-level spectrum is gapped and the chemical potential is in the middle of the gap. However, the gap closes at $k_z = 0$ whenever $\Delta = \hbar\omega_c(n+1/2)$ for quadratic in-plane dispersion, and $\Delta = \hbar\omega_c\sqrt{(n+1/2)}$ for linear in-plane dispersion. Note that the above gap-closure condition is nothing but the equality between the area of the nodal loop $\mathcal{A}_{\mathrm{NL}}$ and the area of the nth quantized magnetic orbit $\mathcal{A}_{\mathrm{B}}(n)$, i.e., $\mathcal{A}_{\mathrm{NL}} = \mathcal{A}_{\mathrm{B}}(n)$, where $\mathcal{A}_{\mathrm{NL}} = \pi\Delta^2/(\hbar^2 v_0^2)$ [$\mathcal{A}_{\mathrm{NL}} = 2\pi m\Delta/(\hbar^2)$] for a nodal loop with linear (quadratic) in-plane dispersions, and the area of nth magnetic orbit $\mathcal{A}_{\mathrm{B}}(n) = 2\pi eB(n+1/2)/\hbar$.

In other words, the Landau levels become gapless whenever the nodal loop exactly overlaps with a quantized magnetic orbit. At the gapless point there expects to be a sharp change in the free energy because a fully occupied Landau level becomes completely unoccupied due to the gap closure and reopening. Thus some singular behavior is expected at the gapless critical point.

To confirm the above conjecture, we calculate the magnetic susceptibility $\chi(B) = -\partial^2 F/\partial B^2$ for the Landau levels shown in Eq. (18) in the limit $\mu \to 0$ and $T \to 0$. It turns out that the magnetic susceptibility consists of a term which diverges logarithmically when the Landau level is gapless:

$$\lim_{\mu\to 0,T\to 0}\chi(B) \sim \frac{e^2\omega_c}{\pi^2\hbar m v_z}\sum_{n=0}^{\infty}(n+1/2)^2\ln\left(\frac{\sqrt{[\Delta/\omega_c-(n+1/2)]^2+\Lambda^2}+\Lambda}{|\Delta/\omega_c-(n+1/2)|}\right) \tag{20}$$

for quadratic–in-plane dispersion, and

$$\lim_{\mu\to 0,T\to 0}\chi(B) \sim \frac{eB}{2\pi^2\hbar}\,\frac{e^2v_0^4}{\omega_c^2}\,\frac{2\Delta}{\omega_c v_z}\sum_{n=0}^{\infty}\sqrt{n+1/2}\ln\left(\frac{\sqrt{(\Delta/\omega_c-\sqrt{n+1/2})^2+\Lambda^2}+\Lambda}{|\Delta/\omega_c-\sqrt{n+1/2}|}\right) \tag{21}$$

for linear in-plane dispersion, where $\Lambda = (\pi v_z)/(\omega_c a)$ is a cutoff parameter with a being the lattice constant on the order of 1 Å. More detailed results about the dHvA quantum oscillations of NLSMs are presented in Appendix F.

The logarithmic divergence indicates a magnetic-field-driven quantum phase transition in the NLSM. In Ref. [25], it was pointed out that the Berry phase of the nth Landau level along the k_z direction would be changed by π through the gap closure at $k_z = 0$, which shows that such a quantum phase transition is indeed a topological one. Here we discuss the nature of such a transition in a bit more detail, and try to make a connection to the transition between two topologically distinct insulating phases in 1D SSH chains. In the SSH model, each energy band is the nondegenerate Bloch band, and the Berry phase is quantized to 0 or π as a result of the chiral symmetry (i.e., there are only intersublattice hoppings in the model) [66]. In our case, the 3D tight-binding model defined in Sec. II (which has a chiral symmetry when $t_0 = 0$) can be reduced to the first line of Eq. (17) after a $\mathbf{k} \cdot \mathbf{p}$ expansion around the high-symmetry $\mathbf{k}$ point about which the nodal loop is centered. Then such a 3D low-energy Hamiltonian is reduced to an effective 1D problem as the in-plane electrons' motions are confined by external magnetic field. The resulted Landau spectra shown in Eq. (18) may be considered as massively degenerate Bloch bands of some effective 1D systems (as there is translational symmetry along z). Then it is meaningful to ask what is the Berry phase of the occupied Landau bands of such an effective 1D system,

$$\phi = \sum_{n,l} \int_{-\pi}^{\pi} dk_z \, i \left\langle \psi_{n,l}(k_z) \middle| \partial_{k_z} \psi_{n,l}(k_z) \right\rangle, \qquad (22)$$

where n is the Landau-level index, and l is the index of the degenerate eigenstate within the nth Landau level, and the summation is restricted to occupied states. We notice that if the original 3D model [Eq. (17) or the tight-binding model introduced in Sec. II] possesses chiral symmetry, then the chiral symmetry should be preserved in the presence of external magnetic field along the z direction (neglecting Zeeman splitting), so that the resulting Landau spectra are exactly symmetric about 0. Thus the argument that applies to the SSH chains can be carried over to such Landau bands with such chiral symmetry, i.e., the Berry phase of the Landau bands expressed in Eq. (22) have to be exactly quantized as 0 or π. In this sense, the transition of two gapped Landau spectra through the band touching at $k_z = 0$ is indeed a topological phase transition, and we have shown that the quantum critical point of the topological transition is characterized by the logarithmic divergence of magnetic susceptibility.

It worthwhile to note that quantum-oscillation behavior is not expected when an in-plane magnetic field is applied. In our simplified model the nodal loop has zero cross section normal to the x or y direction, so that Landau levels cannot be formed for in-plane magnetic fields. It implies that Zeeman splitting would dominate over orbital effects for in-plane magnetic fields, and the spin-degenerate nodal loop might be splitted into a pair of nondegenerate "Weyl loops," or splitted into pairs of isolated Weyl nodes. In realistic systems, the nodal loop is not necessarily confined within the k_x-k_y plane, so quantum oscillations with in-plane magnetic fields are allowed, but the period is expected to be much larger than that when the magnetic field is along the z direction.

VI. CONCLUSION

To summarize, we have studied the effects of Hubbard interactions and bulk quantum oscillations in NLSMs. Our HF calculations indicate that Hubbard interactions tend to drive the system into surface-ordered phases through quantum phase transitions at the surface. In particular, in the absence of surface Rashba SOC, the system becomes ferromagnetic at the surface at small U, and enters into a surface charge-ordered phase at slightly increased U through a first-order transition. On the other hand, surface Rashba SOC splits the otherwise twofold degenerate drumhead surface states and endows them with nontrivial spin textures, so that a surface canted FM phase becomes stable for moderate U values. The quantum critical behavior of the surface ferromagnetic transition is distinct from that in conventional 2D or 3D metals. This is due to Landau damping of the 2D spin fluctuations into electron-hole excitations near the nodal loop in the third dimension. This "mixed dimensionality" of the system is argued to result in a modified dynamical critical exponent, with $z \approx 1$ at the level of a Hertz-Millis analysis, when the Fermi level is close to the bulk nodal energy. We have also studied the bulk quantum oscillations of NLSMs in the noninteracting case, and find that in the limit of zero temperature and zero chemical potential, there is a logarithmic divergence in the magnetic susceptibility whenever the nodal loop overlaps with a quantized magnetic orbit. Such a logarithmic divergence is accompanied by the gap closure of the Landau levels, and is periodic in $1/B$. The predictions of interaction-driven surface ordering and bulk quantum oscillations may stimulate future experimental and theoretical studies of NLSMs.

Note added. Recently we became aware of three related works by Pal *et al.* [67], Roy [68], and Pamuk *et al.* [69]. Pal *et al.* have thoroughly studied the quantum-oscillation behaviors of various physical quantities in a model of two-dimensional valence and conduction bands that touch along a loop, and in this context explored the temperature dependence of the quantum oscillations. Roy has discussed effects of Coulomb interactions in the bulk of nodal-loop semimetals. Pamuk *et al.* have performed first-principles calculations on slabs of rhombohedral graphite (which has been proposed to be a bulk nodal-loop metal [70]), and found interesting ferrimagnetic spin order localized at the surface.

ACKNOWLEDGMENTS

J.L. would like to thank S. Y. Park for his education on the linear-tetrahedron method. This work was supported by the National Science Foundation under Grant No. NSF DMR1506119.

APPENDIX A: SELF-CONSISTENT HARTREE-FOCK APPROXIMATION

In Sec. III, the self-consistent Hartree-Fock (HF) approximation is adopted to calculate the ground states of the interacting Hamiltonians, i.e.,

$$U\hat{n}_{l\uparrow}\hat{n}_{l\downarrow} \rightarrow U\langle\hat{n}_{l\uparrow}\rangle\hat{n}_{l\downarrow} + U\hat{n}_{l\uparrow}\langle\hat{n}_{l\downarrow}\rangle - U\langle\hat{n}_{l\uparrow}\rangle\langle\hat{n}_{l\downarrow}\rangle, \qquad (A1)$$

where $\hat{n}_{l\sigma}$ refers to the density operator of electrons with spin σ ($\sigma = \uparrow,\downarrow$) at site l, $\langle\hat{n}_{l\sigma}\rangle$ is the self-consistent mean field applied to the electrons of spin $-\sigma$ at site l; U denotes the amplitude of the Hubbard repulsion. The linear tetrahedron method [71] is implemented as an interpolation scheme so that the self-consistent calculations can be carried out with improved numeric efficiency.

Including SOC, the noncollinear HF is slightly more complicated than its collinear version:

$$U n_{l\uparrow} n_{l\downarrow} \to U[c^{\dagger}_{l\uparrow}, c^{\dagger}_{l\downarrow}](\langle n_l\rangle - \mathbf{m}_l\cdot\mathbf{s}_l)[c_{l\uparrow}, c_{l\downarrow}]^T \\ - U\langle n_{l\uparrow}\rangle\langle n_{l\downarrow}\rangle + U\langle c^{\dagger}_{l\uparrow}c_{l\downarrow}\rangle\langle c^{\dagger}_{l\downarrow}c_{l\uparrow}\rangle, \quad \text{(A2)}$$

where $c^{\dagger}_{l\uparrow(\downarrow)}$ ($c_{l\uparrow(\downarrow)}$) represents the creation (annihilation) operator of electrons at site i with ↑ (↓) denoting electrons' spins. $n_{l\sigma} = c^{\dagger}_{l\sigma}c_{l\sigma}$ ($\sigma = \uparrow,\downarrow$) is the number operator at site i with spin σ, and $n_l = n_{l\uparrow} + n_{l\downarrow}$ is the total number operator. $\langle\ldots\rangle$ represents the expectation value of some operator in the HF ground state. $\mathbf{s}_l = [s^x_l, s^y_l, s^z_l]$ are the Pauli matrices representing an electron's spin at site l, which couples to the self-consistent vector field $\mathbf{m}_l = [m^x_l, m^y_l, m^z_l]$, where

$$m^x_l = \langle c^{\dagger}_{l\uparrow}c_{l\downarrow} + c^{\dagger}_{l\downarrow}c_{l\uparrow}\rangle, \\ m^y_l = i\langle c^{\dagger}_{l\downarrow}c_{l\uparrow} - c^{\dagger}_{l\uparrow}c_{l\downarrow}\rangle, \\ m^z_l = \langle c^{\dagger}_{l\uparrow}c_{l\uparrow} - c^{\dagger}_{l\downarrow}c_{l\downarrow}\rangle, \quad \text{(A3)}$$

APPENDIX B: GENERALIZED RPA SUSCEPTIBILITY

The generalized susceptibility in the random-phase approximation (RPA) χ^{RPA} can be expressed as [55]

$$\chi^{\text{RPA}} = (1 - \chi^{(0)}\mathbb{U})^{-1}\chi^{(0)}, \quad \text{(B1)}$$

where $\chi^{(0)}$ and $\mathbb{U}$ are the matrices representing the bare susceptibility and the Coulomb interactions respectively. To be specific, the bare susceptibility can be calculated from the noninteracting Green's function,

$$\chi^{(0)}_{\alpha\beta l,\alpha'\beta' l'}(\mathbf{q}, i\nu_n) = -k_{\text{B}}T\int\frac{dk^2}{(2\pi)^2}\sum_{i\omega_n}G^{(0)}_{\alpha' l',\alpha l}(\mathbf{k}, i\omega_n) \\ \times G^{(0)}_{\beta l,\beta' l'}(\mathbf{k}+\mathbf{q}, i\omega_n + i\nu_n), \quad \text{(B2)}$$

where the α, α', β, and β' are the spin indices, while l and l' label the lattice sites in the slab; $\mathbf{k}$ is the wave vector of the noninteracting Bloch functions, and the sum over Matsubara frequency ω_n can be taken analytically in the basis that diagonalizes the noninteracting Hamiltonian at each $\mathbf{k}$. k_{B} is the Boltzmann constant and T is the temperature; $k_{\text{B}}T$ is fixed as 1/100 in the RPA calculations in Sec. III. Note that in the nonordered phase without spin-orbit coupling, all kinds of spin fluctuations are equivalent to each other, i.e., $\chi^{(0)}_{\uparrow\uparrow l,\uparrow\uparrow l'} = \chi^{(0)}_{\uparrow\downarrow l,\uparrow\downarrow l'} = \chi^{(0)}_{\downarrow\uparrow l,\downarrow\uparrow l'} = \chi^{(0)}_{\downarrow\downarrow l,\downarrow\downarrow l'}$. With SOC included, terms like $\chi^{(0)}_{\uparrow\uparrow l,\downarrow\downarrow l'}$ are also allowed, and spin fluctuations become anisotropic.

The interaction matrix for Hubbard interactions is defined as

$$\mathbb{U}^{l,l'}_{\beta\alpha',\alpha\beta'} = -(U\delta_{l,l'}\delta_{\beta'\alpha'}\delta_{\beta\alpha}\delta_{\alpha,-\alpha'} - U\delta_{l,l'}\delta_{\alpha\beta'}\delta_{\beta\alpha'}\delta_{\alpha,-\beta}). \quad \text{(B3)}$$

The over minus sign on the right-hand side (RHS) of Eq. (B3) is from the minus sign in the time-ordered exponential of the S matrix [57]. The first term on the RHS of Eq. (B3) represents a direct Coulomb interaction, while the second term is the exchange interaction. Then the matrix element of the static RPA spin susceptibilities are expressed as

$$\chi^{\text{RPA}}_{zz}(\mathbf{q})_{l,l'} = \chi^{\text{RPA}}(\mathbf{q})_{\uparrow\uparrow l,\uparrow\uparrow l'} - \chi^{\text{RPA}}(\mathbf{q})_{\downarrow\downarrow l,\uparrow\uparrow l'} \\ - \chi^{\text{RPA}}(\mathbf{q})_{\uparrow\uparrow l,\downarrow\downarrow l'} + \chi^{\text{RPA}}(\mathbf{q})_{\downarrow\downarrow l,\downarrow\downarrow l'}, \\ \chi^{\text{RPA}}_{xx}(\mathbf{q})_{l,l'} = \chi^{\text{RPA}}(\mathbf{q})_{\uparrow\downarrow l,\uparrow\downarrow l'} + \chi^{\text{RPA}}(\mathbf{q})_{\downarrow\uparrow l,\uparrow\downarrow l'} \\ + \chi^{\text{RPA}}(\mathbf{q})_{\uparrow\downarrow l,\downarrow\uparrow l'} + \chi^{\text{RPA}}(\mathbf{q})_{\downarrow\uparrow l,\downarrow\uparrow l'}, \\ \chi^{\text{RPA}}_{yy}(\mathbf{q})_{l,l'} = \chi^{\text{RPA}}(\mathbf{q})_{\uparrow\downarrow l,\uparrow\downarrow l'} - \chi^{\text{RPA}}(\mathbf{q})_{\downarrow\uparrow l,\uparrow\downarrow l'} \\ - \chi^{\text{RPA}}(\mathbf{q})_{\uparrow\downarrow l,\downarrow\uparrow l'} + \chi^{\text{RPA}}(\mathbf{q})_{\downarrow\uparrow l,\downarrow\uparrow l'}. \quad \text{(B4)}$$

The eigenvalues of $\chi^{\text{RPA}}_{zz}(\mathbf{q})$ at $t_2 = t_1$ and $U = 0.25t_1$ (t_1 and t_2 are defined in Sec. II) are shown in Fig. 4(a). As discussed in Sec. III, the surface modes of $\chi^{\text{RPA}}_{zz}(\mathbf{q})$ are much stronger than the bulk modes, and tend to diverge at $\overline{\Gamma}$ as U approaches some critical value U_c indicating a continuous quantum phase transition at the surface. The surface modes of the in-plane RPA spin susceptibilities $\chi^{\text{RPA}}_{xx}(\mathbf{q})$ and $\chi^{\text{RPA}}_{yy}(\mathbf{q})$ are shown in Fig. 5.

APPENDIX C: SURFACE GREEN'S FUNCTION

In this section we derive the surface Green's function of NLSMs using the method reported in Ref. [63]. To be specific, using the Dyson equation, the surface Green's function $G_s(\mathbf{k}_{\parallel}, \omega)$ can be expressed as

$$G_s = G_0 + G_0 V G_s, \quad \text{(C1)}$$

where G_s is the full surface Green's function with the corresponding Hamiltonian H, $V = H - H_0$ is the potential difference between a crystal with and without a surface, and G_0 is the noninteracting bulk Green's function. In the basis of the "hybrid Wannier functions" [72] which are extended in the x-y plane and localized in the z direction, Eq. (C1) can be written as

$$G_s(\mathbf{k}_{\parallel}, \omega) = G_0(\mathbf{k}_{\parallel}, \omega; 0) + G_0(\mathbf{k}_{\parallel}, \omega; 1)V(-1,0)G_s(\mathbf{k}_{\parallel}, \omega), \quad \text{(C2)}$$

where $G_0(\mathbf{k}_{\parallel}, \omega; l)$ (l is an integer labeling the primitive cells in the z direction) is the bulk Green's function defined in the hybrid Wannier function basis:

$$G_0(\mathbf{k}_{\parallel}, \omega; l) = \int\frac{dk_z}{2\pi}e^{ik_z l}G_0(\mathbf{k}, \omega), \quad \text{(C3)}$$

and the bulk Green's function $G_0(\mathbf{k}, \omega)$ is

$$G_0(\mathbf{k}, \omega) = \frac{-\widetilde{\omega}\,\mathbb{I}_{2\times 2} - (\widetilde{t}_1 + t_2\cos k_z)\,\tau_x - t_2\sin k_z\,\tau_y}{\widetilde{t}_1^2 + t_2^2 + 2\widetilde{t}_1 t_2\cos k_z - t_2^2\,\widetilde{\omega}^2} \quad \text{(C4)}$$

In the above equation $\mathbb{I}_{2\times 2}$ is the 2 × 2 identity matrix, τ_x, τ_y, and τ_z are the Pauli matrices defined in the sublattice space. $\widetilde{t}_1$ and $\widetilde{\omega}$ are defined in Eq. (2) in Sec. IV. If the bulk tight-binding model introduced in Sec. II is truncated at sublattice A with an ideal surface termination, the surface perturbation potential $V(-1,0)$ can be expressed as

$$V(-1,0) = \begin{pmatrix} 0 & 0 \\ -t_2 & 0 \end{pmatrix}. \quad \text{(C5)}$$

Plugging Eqs. (C3)–(C5) into Eq. (C2), one obtains

$$G_s(\mathbf{k}_\parallel,\omega)_{1,1} = \frac{G_0(\mathbf{k}_\parallel,\omega;0)_{1,1}}{1+t_2G_0(\mathbf{k}_\parallel,\omega;1)_{1,2}}, \tag{C6}$$

where

$$G_0(\mathbf{k}_\parallel,\omega;1)_{1,2} = -\int_{k_z} e^{ik_z}\frac{\tilde{t}_1+t_2e^{-ik_z}}{\tilde{t}_1^2+t_2^2+2\tilde{t}_1t_2\cos k_z - t_2^2\,\tilde{\omega}^2}, \tag{C7}$$

and

$$G_0(\mathbf{k}_\parallel,\omega;0)_{1,1} = \int_{k_z}\frac{-t_2\,\tilde{\omega}}{\tilde{t}_1^2+t_2^2+2\tilde{t}_1t_2\cos k_z - t_2^2\,\tilde{\omega}^2}, \tag{C8}$$

where $\int_{k_z} = \int_0^{2\pi} dk_z/(2\pi)$. Again, $\tilde{\omega}$ is defined in Eq. (2). Defining $\eta = e^{ik_z}$, the integral over k_z in Eq. (C7) can be replaced by a contour integral around a unit circle in the complex plane of η, and can be solved exactly:

$$G_0(\mathbf{k}_\parallel,\omega;1)_{1,2} = -\frac{\tilde{t}_1\eta_+ + t_2}{\tilde{t}_1t_2(\sqrt{\gamma^2-4})}, \tag{C9}$$

and

$$G_0(\mathbf{k}_\parallel,\omega;0)_{1,1} = -\frac{t_2\,\tilde{\omega}}{\tilde{t}_1t_2}\frac{1}{\sqrt{\gamma^2-4}}, \tag{C10}$$

where

$$\gamma = \left(\tilde{t}_1^2+t_2^2-t_2^2\,\tilde{\omega}^2\right)/(\tilde{t}_1t_2), \tag{C11}$$

and

$$\eta_+ = (-\gamma+\sqrt{\gamma^2-4})/2. \tag{C12}$$

From Eq. (C9) one may notice that $G_0(\mathbf{k}_\parallel,\omega;1)_{1,2}$ is real only if $\gamma^2-4>0$, which implies that $G_s(\mathbf{k}_\parallel,\omega)_{1,1}$ may have a pole on the real axis only when $\gamma^2-4>0$. It follows that $\gamma^2-4=0$ defines the bulk spectral edge: when $\gamma^2-4<0$, ω is in the bulk continuum; while when $\gamma^2-4>0$, ω is in the bulk gap and there may be bound-state solutions. Then it is straightforward to show that

$$\begin{aligned} &\text{if}\quad -\left|k_\parallel^2-k_0^2\right| < \tilde{\omega} < \left|k_\parallel^2-k_0^2\right|, \quad \omega\text{ in the bulk gap},\\ &\text{if}\quad \tilde{\omega} > \left|k_\parallel^2-k_0^2\right| \text{ or } \tilde{\omega} < -\left|k_\parallel^2-k_0^2\right|, \quad \omega\text{ in the bulk continuum,} \end{aligned} \tag{C13}$$

where k_0 characterizing the size of the nodal loop is defined in Eq. (4), and $\tilde{\omega}$ is defined in Eq. (2).

Plugging Eqs. (C9) and (C10) into Eq. (C6), we obtain

$$G_s(\mathbf{k}_\parallel,\omega) = \frac{-\tilde{\omega}}{\tilde{t}_1}\frac{1}{(\sqrt{\gamma^2-4}+\gamma)/2 - t_2/\tilde{t}_1}. \tag{C14}$$

Plugging $\tilde{t}_1 = t_2(1+k_\parallel^2-k_0^2)$ into Eq. (C11), considering the low-energy excitations around the nodal loop so that $k_\parallel^2-k_0^2$ and $\tilde{\omega}$ are small, one obtains the final expression of the surface Green's function shown in Eq. (1) by dropping some terms higher order in $k_\parallel^2-k_0^2$ and $\tilde{\omega}$.

When ω is in the bulk gap, Eq. (1) can be re-expressed as

$$\begin{aligned} G_s(k_\parallel,\omega) &= \frac{-\tilde{\omega}}{t_2}\frac{1}{\left(\sqrt{\left(k_\parallel^2-k_0^2\right)^2-\tilde{\omega}^2}+k_\parallel^2-k_0^2\right)}\\ &\approx \frac{-\tilde{\omega}}{t_2}\frac{1}{\left\{\left|k_\parallel^2-k_0^2\right|\left[1-\tilde{\omega}^2/\left(k_\parallel^2-k_0^2\right)^2\right]+k_\parallel^2-k_0^2\right\}}. \end{aligned} \tag{C15}$$

From the above equation we see that for $k_\parallel < k_0$,

$$G_s(k_\parallel,\omega) \approx \frac{\left(k_0^2-k_\parallel^2\right)}{t_2\,\tilde{\omega}}, \tag{C16}$$

corresponding to the drumhead surface states at $\tilde{\omega}=0$.

From the above analysis we see that when the surface is terminated at sublattice A there are drumhead surface states with dispersion $t_0(k_\parallel^2-k_0^2)$ inside the projected nodal loop. On the other hand, when the surface is terminated at sublattice B, the role of $\tilde{t}_1$ and t_2 is interchanged, so that there are drumhead surface states only when $\tilde{t}_1 > t_2$, i.e., outside the projected nodal loop ($k_\parallel > k_0$). This explains the termination-dependent surface states as shown in Figs. 2(a) and 2(b).

APPENDIX D: DERIVATIONS OF SURFACE DYNAMICAL SUSCEPTIBILITY

1. Derivations of Eqs. (12) and (13)

We first derive the low-energy, long-wavelength behavior of the surface dynamical susceptibility of a hole-doped NLSM contributed by the extended bulk states projected at the surface, which are expressed by Eqs. (12) and (13) in Sec. IV. Such contributions are labeled as "$b-b$" in Fig. 6(a). In principle we need to calculate the imaginary part of $\chi_{bb}(\mathbf{q}_\parallel,\nu,\mu)$ which is expressed in Eq. (11).

Again, we consider the situation that the nodal loop is centered at (π,π,π) whose size is small compared to the BZ. Then we expand $\tilde{t}_1$ around (π,π) up to quadratic order of $k_\parallel$ as shown in Eq. (3). Since we are interested in Fermi-surface fluctuations from the bulk continuum, we neglect the dispersion from t_0, so the spectral density of the bulk continuum f_b becomes

$$f_b(\mathbf{k}_\parallel,\epsilon) \approx \frac{\sqrt{\epsilon^2-x_{\mathbf{k}_\parallel}^2}}{\epsilon}\theta(|\epsilon|-|x_{\mathbf{k}_\parallel}|). \tag{D1}$$

Without loss of generality, the Bosonic wave vector $\mathbf{q}_\parallel$ is chosen to point along the x direction, $\mathbf{q}_\parallel = (q_\parallel,0)$. Then we define

$$x_{\mathbf{k}_\parallel} = k_\parallel^2 - k_0^2. \tag{D2}$$

We also define

$$\widetilde{\mu} = \mu/t_2, \quad \widetilde{\nu} = \nu/t_2, \quad \widetilde{t}_0 = t_0/t_2. \tag{D3}$$

Plugging the expression of f_b in Eq. (D1) into Eq. (11), one obtains

$$\begin{aligned}
\mathrm{Im}\,\chi(\mathbf{q}_\parallel,\nu,\mu) &= \int_{\mathbf{k}_\parallel}\int_{-\widetilde{\mu}}^{-\widetilde{\mu}+\widetilde{\nu}} d\epsilon\, \frac{\sqrt{\epsilon^2 - x_{\mathbf{k}_\parallel}^2}\sqrt{(\widetilde{\nu}-\epsilon)^2 - x_{\mathbf{k}_\parallel+\mathbf{q}_\parallel}^2}}{-\epsilon(\widetilde{\nu}-\epsilon)}\,\theta(|\epsilon| - |x_{\mathbf{k}_\parallel}|)\,\theta(|\nu-\epsilon| - |x_{\mathbf{k}_\parallel+\mathbf{q}_\parallel}|)\\
&= \int_{-\widetilde{\mu}}^{-\widetilde{\mu}+\widetilde{\nu}} d\epsilon \int_{-\epsilon}^{\epsilon} dx \int_{-(\epsilon-\widetilde{\nu})/(2k_0q_\parallel)}^{(\epsilon-\widetilde{\nu})/(2k_0q_\parallel)} dy\, \frac{2k_0q_\parallel\sqrt{\epsilon^2-x^2}\sqrt{(\widetilde{\nu}-\epsilon)^2/\big(4k_0^2q_\parallel^2\big) - y^2}}{-\epsilon(\widetilde{\nu}-\epsilon)\sqrt{1-[\,y-(x+q_\parallel^2)/(2k_0q_\parallel)]^2}}\\
&\approx \int_{-\widetilde{\mu}}^{-\widetilde{\mu}+\widetilde{\nu}} d\epsilon \int_{-\epsilon}^{\epsilon} dx \int_{-(\epsilon-\widetilde{\nu})/(2k_0q_\parallel)}^{(\epsilon-\widetilde{\nu})/(2k_0q_\parallel)} dy\, \frac{2k_0q_\parallel\sqrt{\epsilon^2-x^2}\sqrt{(\widetilde{\nu}-\epsilon)^2/\big(4k_0^2q_\parallel^2\big) - y^2}}{-\epsilon(\widetilde{\nu}-\epsilon)}\\
&= \int_{-\widetilde{\mu}}^{-\widetilde{\mu}+\widetilde{\nu}} d\epsilon \int_{-\epsilon}^{\epsilon} dx\, \frac{\sqrt{\epsilon^2-x^2}(\epsilon-\widetilde{\nu})}{2k_0q_\parallel\epsilon}\\
&= \int_{-\widetilde{\mu}}^{-\widetilde{\mu}+\widetilde{\nu}} d\epsilon\, \frac{\epsilon(\epsilon-\widetilde{\nu})}{2k_0q_\parallel}\int_{-1}^{1} dx'\sqrt{1-x'^2}\\
&= \frac{\pi}{4k_0q_\parallel}(\epsilon^3/3 - \widetilde{\nu}\epsilon^2/2)\Big|_{-\widetilde{\mu}}^{-\widetilde{\mu}+\widetilde{\nu}}\\
&= \frac{\pi}{4k_0q_\parallel}(\widetilde{\mu}^2\widetilde{\nu} - \widetilde{\nu}^3/6),
\end{aligned} \tag{D4}$$

where the second line of the above equation follows due to the heaviside θ function, and $y = (x + q_\parallel^2)/(2k_0q_\parallel) + \cos\phi$, with ϕ being the angle between $\mathbf{k}_\parallel$ and $\mathbf{q}_\parallel$. We have made the approximation that $\sqrt{1-[\,y-(x+q_\parallel^2)/(2k_0q_\parallel)]^2} \approx 1$ when going from the second to the third line in Eq. (D4). The fourth line of Eq. (D4) follows by using the integral identity:

$$\int_{-b}^{b} dy\sqrt{b^2-y^2} = \frac{\pi}{2}b^2, \tag{D5}$$

where $b = (\epsilon - \widetilde{\nu})/(2k_0q_\parallel)$. Finally in the fifth line we define $\epsilon x' = x$, and it follows that $\mathrm{Im}\,\chi_{bb}(\mathbf{q}_\parallel,\nu,\mu) \sim \nu/q_\parallel$. Equation (12) is proved.

As discussed in the main text, the surface susceptibility is a nonvanishing even at $\mathbf{q}_\parallel = 0$ due to the bulk fluctuations. As expressed in Eq. (13), $\mathrm{Im}\,\chi(q_\parallel = 0,\nu,\mu) \sim \nu$ for $\mu < 0$. Using some similar tricks as those in Eq. (D4), it is straightforward to show that when $q_\parallel = 0$,

$$\begin{aligned}
&\mathrm{Im}\,\chi(q_\parallel = 0,\nu,\mu)\\
&\quad = 2\pi\int_{-\widetilde{\mu}}^{-\widetilde{\mu}+\widetilde{\nu}} d\epsilon \int_{-1}^{1} dx'\,(\epsilon-\widetilde{\nu})\\
&\quad\quad \times \sqrt{1-x'^2}\sqrt{1-(1-\widetilde{\nu}/\epsilon)^2x'^2}\\
&\quad \approx \frac{4}{3}\pi(|\widetilde{\mu}|\,\widetilde{\nu} - \widetilde{\nu}^2/2),
\end{aligned} \tag{D6}$$

where the integral over x' is approximated by a constant $2/3$. Such an approximation is valid as long as the frequency is much smaller than the Fermi level, i.e., $\nu \ll |\mu|$. Thus Eq. (13) is proved.

2. Derivations of Eqs. (15) and (16)

Now we turn to the case of Fig. 6(b), i.e., the surface bands are filled and the electron-hole excitations are mostly contributed by the $b - b$ and $s - b$ processes.

Let us first consider the $b - b$ process. Since we are interested in the bulk-state fluctuations, we neglect the dispersions from t_0 in the bulk continuum spectral density, i.e., $\widetilde{\omega} \approx \omega/t_2$, and Eq. (D1) applies. One may still use Eq. (D4), except that now the Fermi level is right at the nodal energy $\mu = 0$. Then it immediately follows from Eq. (D4) that $\mathrm{Im}\,\chi(\mathbf{q}_\parallel,\nu,\mu = 0) \sim \nu^3/q_\parallel$, which proves Eq. (15).

Next we consider the process that an electron is created in the bulk conduction band and a hole is left in the otherwise occupied surface bands as denoted by $s - b$ in Fig. 6(b). Let us consider a simplified case that $t_0 = 0$ so that the surface bands are perfectly flat and completely occupied. Then,

$$\begin{aligned}
f_b(\mathbf{k}_\parallel,\epsilon) &\approx \frac{\sqrt{\epsilon^2 - x_{k_\parallel}^2}}{\epsilon}\,\theta\,(|\epsilon| - |x_{k_\parallel}|),\\
f_s(\mathbf{k}_\parallel,\epsilon) &\approx |x_{k_\parallel}|\,\delta(\epsilon)\,\theta(-x_{k_\parallel}).
\end{aligned} \tag{D7}$$

Plugging the above equation into Eq. (16), one obtains

$$
\begin{aligned}
\operatorname{Im}\chi_{\rm sb}(\mathbf{q}_\parallel,\nu,\mu=0) &= \int_{\mathbf{k}_\parallel}\int_0^{\widetilde{\nu}} d\epsilon\, f_s(-\epsilon,\mathbf{k}_\parallel-\mathbf{q}_\parallel)\, f_b(\widetilde{\nu}-\epsilon,\mathbf{k}_\parallel)\\
&= \int_{\mathbf{k}_\parallel}\int_0^{\widetilde{\nu}} d\epsilon |x_{\mathbf{k}_\parallel-\mathbf{q}_\parallel}|\,\delta(-\epsilon)\,\theta(-x_{\mathbf{k}_\parallel-\mathbf{q}_\parallel})\,\frac{\sqrt{(\widetilde{\nu}-\epsilon)^2-x_{\mathbf{k}_\parallel}^2}}{\widetilde{\nu}-\epsilon}\theta(|\widetilde{\nu}-\epsilon|-|x_{\mathbf{k}_\parallel}|)\\
&\approx \int_{-\widetilde{\nu}}^{\widetilde{\nu}} dx \int_{(x+q_\parallel^2)/(2k_0q_\parallel)}^{1} \frac{d\cos\phi}{\sqrt{1-\cos^2\phi}}\left(2q_\parallel\cos\phi\sqrt{k_0^2+x}-x-q_\parallel^2\right)\frac{\sqrt{\widetilde{\nu}^2-x^2}}{\widetilde{\nu}}\\
&= 2q_\parallel k_0\int_{-\widetilde{\nu}}^{\widetilde{\nu}} dx\,\frac{\sqrt{\widetilde{\nu}^2-x^2}}{\widetilde{\nu}}\sqrt{1-(x+q_\parallel^2)^2/\big(4k_0^2q_\parallel^2\big)}-\int_{-\widetilde{\nu}}^{\widetilde{\nu}}\frac{\sqrt{\widetilde{\nu}^2-x^2}}{\widetilde{\nu}}(x+q_\parallel^2)\int_{(x+q_\parallel^2)/(2k_0q_\parallel)}^{1}\frac{d\cos\phi}{\sqrt{1-\cos^2\phi}}\\
&\approx 2q_\parallel k_0\int_{-\widetilde{\nu}}^{\widetilde{\nu}} dx\,\frac{\sqrt{\widetilde{\nu}^2-x^2}}{\widetilde{\nu}}\sqrt{1-(x+q_\parallel^2)^2/\big(4k_0^2q_\parallel^2\big)}\approx 2q_\parallel k_0\int_{-\widetilde{\nu}}^{\widetilde{\nu}} dx\,\frac{\sqrt{\widetilde{\nu}^2-x^2}}{\widetilde{\nu}}=\pi k_0q_\parallel\widetilde{\nu}.
\end{aligned}
\tag{D8}
$$

In the above equation, $x\equiv x_{\mathbf{k}_\parallel}=k_\parallel^2-k_0^2$, and we have made the approximation $x_{\mathbf{k}_\parallel-\mathbf{q}_\parallel}=(|\mathbf{k}_\parallel-\mathbf{q}_\parallel|)^2-k_0^2\approx x+q_\parallel^2-2k_0q_\parallel\cos\phi$. We have used the integral identity, $\int dx(1/\sqrt{1-x})=-2\sqrt{1-x}$, when going from the third to the fourth line, and we have dropped the second term on the right-hand side of the fourth line because it is higher order, $\sim q_\parallel^2\widetilde{\nu}$ or $\sim\widetilde{\nu}^2q_\parallel$. Finally we have made the approximation $\sqrt{[1-(x+q_\parallel^2)^2/(4k_0^2q_\parallel^2)]}\approx 1$ from the fifth to the six line. We see that the final result presented in Eq. (D8) is consistent with Eq. (16) in the main text when $t_0=0$. It follows that when the $\mu=0$, the $s-b$ process dominates over the $b-b$ process, and leads to a dynamical critical exponent $z\approx 1$.

Now we consider the case of nonvanishing t_0, i.e., the surface bands are not perfectly flat, but with a bandwidth $\sim t_0$. Plugging Eq. (8) into Eq. (16), then integrating over ϵ, one obtains

$$
\begin{aligned}
&\operatorname{Im}\chi_{\rm sb}(\mathbf{q}_\parallel,\nu,\mu=0)\\
&\quad=\int_{\mathbf{k}_\parallel}|x_{\mathbf{k}_\parallel-\mathbf{q}_\parallel}|\,\theta(-x_{\mathbf{k}_\parallel-\mathbf{q}_\parallel})\,\theta(|\widetilde{\nu}+\widetilde{t}_0x_{\mathbf{k}_\parallel-qp}|)\\
&\quad\quad\times\frac{\sqrt{(\widetilde{\nu}+\widetilde{t}_0x_{\mathbf{k}_\parallel-\mathbf{q}_\parallel})^2-x_{\mathbf{k}_\parallel}^2}}{\widetilde{\nu}+\widetilde{t}_0x_{\mathbf{k}_\parallel-\mathbf{q}_\parallel}},
\end{aligned}
\tag{D9}
$$

where $x_{\mathbf{k}_\parallel}$ is defined in Eq. (D2). Let us define $x\equiv x_{\mathbf{k}_\parallel}$ and $y\equiv x_{\mathbf{k}_\parallel-\mathbf{q}_\parallel}$. Since x is around 0, we make the following approximation to y:

$$
\begin{aligned}
y&=x_{\mathbf{k}_\parallel-\mathbf{q}_\parallel}\\
&=x-2\sqrt{x^2+k_0^2}\,q_\parallel\cos\phi+q_\parallel^2\\
&\approx x-2k_0q_\parallel\cos\phi+q_\parallel^2.
\end{aligned}
\tag{D10}
$$

Plugging Eq. (D10) into Eq. (D9), and imposing the constraints on the limits of integrations from the two Heaviside θ functions, one obtains

$$
\begin{aligned}
&\operatorname{Im}\chi_{\rm sb}(\mathbf{q}_\parallel,\nu,\mu=0)\\
&\quad=\int_{x-2k_0q_\parallel+q_\parallel^2}^{0}\frac{dy}{2k_0q_\parallel}\int_{-|\widetilde{\nu}+\widetilde{t}_0y|}^{|\widetilde{\nu}+\widetilde{t}_0y|}\sqrt{(\widetilde{\nu}+\widetilde{t}_0y)^2-x^2}\,\frac{-y}{\widetilde{\nu}+\widetilde{t}_0y}
\end{aligned}
$$

$$
\approx-\frac{\pi}{4k_0q_\parallel}\int_{-2k_0q_\parallel+q_\parallel^2}^{0}dy\,y\,(\widetilde{\nu}+\widetilde{t}_0y),
\tag{D11}
$$

where the second line of the above equation follows due to the following approximation on the limit of integration of y:

$$
\int_{x-2k_0q_\parallel+q_\parallel^2}^{0}\to\int_{-2k_0q_\parallel+q_\parallel^2}^{0},
\tag{D12}
$$

and we have used the integral identity

$$
\int_{-|\widetilde{\nu}+\widetilde{t}_0y|}^{|\widetilde{\nu}+\widetilde{t}_0y|}dx\sqrt{(\widetilde{\nu}+\widetilde{t}_0y)^2-x^2}=\frac{\pi(\widetilde{\nu}+\widetilde{t}_0y)^2}{2}.
\tag{D13}
$$

Now we need to discuss two different situations: $\widetilde{\nu}+\widetilde{t}_0y>0$, and $\widetilde{\nu}+\widetilde{t}_0y<0$. If $\widetilde{\nu}+\widetilde{t}_0y>0$, it follows from Eq. (D11) that

$$
\operatorname{Im}\chi_{\rm sb}^{>}(\mathbf{q}_\parallel,\nu)=\frac{\pi\widetilde{\nu}^3}{24k_0q_\parallel}.
\tag{D14}
$$

If $\widetilde{\nu}+\widetilde{t}_0y<0$, it turns out that

$$
\operatorname{Im}\chi_{\rm sb}^{<}(\mathbf{q}_\parallel,\nu)\approx-\frac{\pi\widetilde{\nu}^3}{24k_0q_\parallel}+\frac{\pi k_0q_\parallel}{2}[\widetilde{\nu}-\eta(t_0,q_\parallel)].
\tag{D15}
$$

Combining the above two equations,

$$
\begin{aligned}
\operatorname{Im}\chi_{\rm sb}(\mathbf{q}_\parallel,\nu)&=\operatorname{Im}\chi_{\rm sb}^{<}(\mathbf{q}_\parallel,\nu)+\operatorname{Im}\chi_{\rm sb}^{>}(\mathbf{q}_\parallel,\nu)\\
&=\frac{\pi k_0q_\parallel}{2}\left(\widetilde{\nu}-\frac{2t_0}{3}(2k_0q_\parallel-q_\parallel^2)\right).
\end{aligned}
\tag{D16}
$$

Equation (D16) has the same analytic behavior as Eq. (D8) when $t_0=0$, although the coefficients differ by a factor of 2. We attribute such a difference in the coefficients to the approximation shown in Eq. (D12), and we believe it is not important because it dose not change the analytic behavior of χ_{sb}. It is also clearly seen from Eq. (D16) that the excitation gap $\eta(t_0,q_\parallel) = 2t_0(2k_0q_\parallel - q_\parallel^2)/3$, which is proportional to t_0 and vanishes as $q_\parallel \to 0$. This is also in agreement with our numeric simulations as shown in Table I.

APPENDIX E: NUMERIC CALCULATIONS OF SURFACE DYNAMICAL SUSCEPTIBILITY IN SLAB GEOMETRY

In this section we explain the technical details in the numerical calculations of the surface dynamical susceptibility for a slab of NLSMs, as shown in Figs. 7 and 8. When both the surface Rashba SOC and Coulomb interactions are neglected, the system can be considered as spinless, and we use l,l' to label the lattice sites in the z direction in a slab of NLSMs. The matrix element of zero-temperature dynamical susceptibility is expressed as

$$\chi_{ll'}(\mathbf{q}_\parallel,\nu) = i\int \frac{dk_x dk_y}{(2\pi)^2}\int \frac{d\omega}{2\pi} G^{(0)}_{l'l}(\mathbf{k}_\parallel,\omega)G^{(0)}_{ll'}(\mathbf{k}_\parallel+\mathbf{q}_\parallel,\omega+\nu), \tag{E1}$$

where the $G^{(0)}(\mathbf{k}_\parallel,\omega)$ is the noninteracting Green's function for a slab of NLSMs which can be expressed in matrix form as follows:

$$G^{(0)}(\mathbf{k}_\parallel,\omega) = V(\mathbf{k}_\parallel)G^{(0)}_{\mathrm{diag}}(\mathbf{k}_\parallel,\omega)V^\dagger(\mathbf{k}_\parallel), \tag{E2}$$

where $G^{(0)}_{\mathrm{diag}}$ is a $2N \times 2N$ (N is the number of primitive cells in the slab, and there are two sublattices in each primitive cell) diagonal matrix whose jth diagonal element $G^{(0)}_{\mathrm{diag}}(\mathbf{k}_\parallel,\omega)_{jj} = 1/[\omega - \epsilon_j(\mathbf{k}_\parallel) + i\delta_{j,\mathbf{k}_\parallel}]$, $\delta_{j,\mathbf{k}_\parallel}$ is an infinitesimal quantity which is greater than (less than) 0 if the eigenenergy $\epsilon_j(\mathbf{k}_\parallel)$ is occupied (unoccupied). $V(\mathbf{k}_\parallel)$ is the eigenvector matrix of the Hamiltonian for the slab at $\mathbf{k}_\parallel$ [denoted by $H_{\mathrm{slab}}(\mathbf{k}_\parallel)$]: $\sum_{l'} H_{\mathrm{slab}}(\mathbf{k}_\parallel)_{l,l'}V_{l',j}(\mathbf{k}_\parallel) = \epsilon_j(\mathbf{k}_\parallel)V_{l,j}(\mathbf{k}_\parallel)$. Then Eq. (E1) becomes

$$\chi_{ll'}(\mathbf{q}_\parallel,\nu) = i\int \frac{dk_x dk_y}{(2\pi)^2}\int_{-\infty}^{\infty} \frac{d\omega}{2\pi}\sum_{j,j'=1}^{2N} \frac{W_{ll'jj'}(\mathbf{k}_\parallel,\mathbf{q}_\parallel)}{[\omega - \epsilon_j(\mathbf{k}_\parallel) + i\delta_{j,\mathbf{k}_\parallel}][\omega + \nu - \epsilon_{j'}(\mathbf{k}_\parallel+\mathbf{q}_\parallel) + i\delta_{j',\mathbf{k}_\parallel+\mathbf{q}_\parallel}]}, \tag{E3}$$

where the spectral weight $W_{ll'jj'}(\mathbf{k}_\parallel,\mathbf{q}_\parallel)$ is defined as

$$W_{ll'jj'}(\mathbf{k}_\parallel,\mathbf{q}_\parallel) = V_{l',j}(\mathbf{k}_\parallel)V^*_{l,j}(\mathbf{k}_\parallel)V_{l,j'}(\mathbf{k}_\parallel+\mathbf{q}_\parallel)V^*_{l',j'}(\mathbf{k}_\parallel+\mathbf{q}_\parallel). \tag{E4}$$

The integration over ω can be carried out by closing the contour in the upper half plane, then Eq. (E3) becomes

$$\chi_{ll'}(\mathbf{q}_\parallel,\nu+i\delta) = \int \frac{dk_x dk_y}{(2\pi)^2}\sum_{j,j'=1}^{2N} \frac{W_{ll'jj'}(\mathbf{k}_\parallel,\mathbf{q}_\parallel)\{\theta[\mu - \epsilon_j(\mathbf{k}_\parallel)] - \theta[\mu - \epsilon_{j'}(\mathbf{k}_\parallel+\mathbf{q}_\parallel)]\}}{\epsilon'_j(\mathbf{k}_\parallel+\mathbf{q}_\parallel) - \epsilon_j(\mathbf{k}_\parallel) - \nu - i\delta}. \tag{E5}$$

If the top-surface layer is labeled as the 0th layer, then the surface susceptibility $\chi_{\mathrm{surf}}(\mathbf{q}_\parallel,\nu) = \chi_{00}(\mathbf{q}_\parallel,\nu)$. The numeric integrations over k_x, k_y are replaced by discrete summations on a 280×280 $\mathbf{k}$ mesh, and the infinitesimal quantity δ is chosen as 0.001 in our numerical calculations. The number of primitive cells in the slab is 500.

APPENDIX F: BULK QUANTUM OSCILLATIONS

In this section we derive the dHvA quantum oscillations of bulk NLSMs neglecting Coulomb interactions. We consider two types of low-energy effective Hamiltonians of NLSMs as shown in Eq. (17). The energies of H_0^{qua} (H_0^{lin}) in Eq. (17) have quadratic (linear) in-plane dispersions. The tight-binding model introduced in Sec. II can be reduced to a $\mathbf{k}\cdot\mathbf{p}$ model around the center of the NLSM that is similar to H_0^{qua}; the terms linear in $\mathbf{k}_\parallel$ are killed by tetragonal symmetry. However, we would like to discuss both situations (H_0^{qua} and H_0^{lin}) for the sake of generality.

Landau levels are formed when a magnetic field is applied along the z direction. The expressions of the Landau levels for H_0^{qua} and H_0^{lin} are shown in Eq. (18). As discussed in Sec. V, the Landau levels become gapless whenever the nodal loop exactly overlaps with a quantized magnetic orbit. It is also mentioned that at the gapless point there is expected to be a sharp change in the free energy and the magnetic susceptibility shows logarithmic divergence at zero temperature and zero Fermi level. In the remaining part of this section, we will explicitly derive the magnetic susceptibilities $\chi(B)$ as expressed in Eqs. (20) and (21).

The free energy of the Landau levels with chemical potential μ is expressed as

$$F = -\frac{eB}{\beta 2\pi^2\hbar}\int_{-\pi}^{\pi} dk_z \sum_{n=0}^{\infty}\sum_{\lambda=\pm} \ln(1 + e^{-[E_\lambda(n,k_z)-\mu]\beta}), \tag{F1}$$

where the $\lambda = \pm$ labels the branch of Landau levels, and the Landau levels $E_\pm(n,k_z)$ are expressed in Eq. (18) for both H_0^{qua} and H_0^{lin}. Summing over λ, Eq. (F1) becomes

$$F = -\frac{eB}{\beta 2\pi^2\hbar}\int_{-\pi}^{\pi} dk_z \sum_{n=0}^{\infty} \ln g(E(n,k_z),\mu,\beta), \tag{F2}$$

where

$$g(E(n,k_z),\mu,\beta) = 1 + e^{-[E(n,k_z)-\mu]\beta} + e^{[E(n,k_z)+\mu]\beta} + e^{2\mu\beta}, \tag{F3}$$

$E(n,k_z) = E_+(n,k_z)$ [see Eq. (18)], and $\beta = 1/(k_\mathrm{B}T)$.

Then it is straightforward to calculate the magnetic susceptibility $\chi(B) = -\partial^2 F/\partial B^2$:

$$\chi(B) = \frac{e}{2\pi^2\hbar}\int_{-\pi}^{\pi} dk_z \sum_{n=0}^{\infty}(h_1 + h_2 + h_3), \tag{F4}$$

where

$$h_1 = h(E(n,k_z),\mu,\beta)\,\frac{\partial E(n,k_z)}{\partial B}, \quad h_2 = B\,h(E(n,k_z),\mu,\beta)\,\frac{\partial^2 E(n,k_z)}{\partial^2 B}, \quad h_3 = B\,\frac{\partial h(E(n,k_z),\mu,\beta)}{\partial E(n,k_z)}\left(\frac{\partial E(n,k_z)}{\partial B}\right)^2. \tag{F5}$$

$h(E(n,k_z),\mu,\beta)$ is defined as follows:

$$h(E(n,k_z),\mu,\beta) = \frac{e^{[E(n,k_z)+\mu]\beta} - e^{-[E(n,k_z)-\mu]\beta}}{1 + e^{[E(n,k_z)+\mu]\beta} + e^{-[E(n,k_z)-\mu]\beta} + e^{2\mu\beta}}. \tag{F6}$$

For NLSMs with quadratic in-plane dispersions, the Landau levels are defined in the first line of Eq. (18). Then the partial derivatives of $E(n,k_z)$ with respect to B are readily obtained:

$$\frac{\partial E(n,k_z)}{\partial B} = \frac{e\,(n+1/2)\,[\omega_c(n+1/2) - \Delta]}{m\sqrt{v^2k_z^2 + [\Delta - \omega_c(n+1/2)]^2}}, \quad \frac{\partial^2 E(n,k_z)}{\partial^2 B} = \frac{e\,(n+1/2)^2\,v^2k_z^2}{m\left\{v^2k_z^2 + [\Delta - \omega_c(n+1/2)]^2\right\}^{3/2}}. \tag{F7}$$

Plugging Eq. (F7) into Eq. (F4), one obtains that when $\mu = 0$ and $\beta \to \infty$ ($T \to 0$), one obtains the expression of the magnetic susceptibility:

$$\begin{aligned}\chi(B) =&\frac{2e^2}{2\pi^2\hbar m}\int_{-\pi}^{\pi} dk_z \sum_{n=0}^{\infty}\frac{\left(n+\frac{1}{2}\right)\left[\omega_c\left(n+\frac{1}{2}\right) - \Delta\right]}{E(n,k_z)}\frac{e^2}{2\pi^2\hbar m}\int_{-\pi}^{\pi} dk_z \sum_{n=0}^{\infty}\left(n+\frac{1}{2}\right)^2\frac{\omega_c}{E(n,k_z)},\\ &-\frac{e^2}{2\pi^2\hbar m}\int_{-\pi}^{\pi} dk_z \sum_{n=0}^{\infty}\left(n+\frac{1}{2}\right)^2\frac{\omega_c\left[\omega_c\left(n+\frac{1}{2}\right) - \Delta\right]^2}{E(n,k_z)^3}.\end{aligned} \tag{F8}$$

The integration over k_z in Eq. (F8) can be carried out as follows:

$$\int_{-\pi}^{\pi} dk_z\frac{1}{E(n,k_z)} = \frac{2}{v}\ln\left(\frac{\sqrt{\left[\left(n+\frac{1}{2}\right) - \frac{\Delta}{\omega_c}\right]^2 + \Lambda^2} + \Lambda}{\left|n+\frac{1}{2} - \frac{\Delta}{\omega_c}\right|}\right), \quad \int_{-\pi}^{\pi} dk_z\frac{1}{E(n,k_z)^3} = \frac{2\Lambda}{v\omega_c^2\left(n+\frac{1}{2}-\frac{\Delta}{\omega_c}\right)^2\sqrt{\left(n+\frac{1}{2}-\frac{\Delta}{\omega_c}\right)^2 + \Lambda^2}}, \tag{F9}$$

where $\Lambda = \pi v/\omega_c$ is a dimensionless cutoff parameter (the in-plane lattice parameter is set to unity).

Plugging Eq. (F9) into Eq. (F8), one obtains

$$\begin{aligned}\chi(B) =&\frac{e^2\omega_c}{2\pi^2\hbar m}\sum_{n=0}^{\infty}\Bigg[\left(n+\frac{1}{2}\right)^2\frac{2}{v}\ln[j(n,\omega_c,\Delta)]\\ &+2\left(n+\frac{1}{2}\right)\left(n+\frac{1}{2}-\frac{\Delta}{\omega_c}\right)\frac{2}{v}\ln[j(n,\omega_c,\Delta)]\\ &-\left(n+\frac{1}{2}\right)^2\frac{2\Lambda}{v\sqrt{\left(n+\frac{1}{2}-\frac{\Delta}{\omega_c}\right)^2+\Lambda^2}}\Bigg],\end{aligned} \tag{F10}$$

where

$$j(n,\omega_c,\Delta) = \frac{\sqrt{\left[\left(n+\frac{1}{2}\right) - \frac{\Delta}{\omega_c}\right]^2 + \Lambda^2} + \Lambda}{\left|n+\frac{1}{2}-\frac{\Delta}{\omega_c}\right|}. \tag{F11}$$

The first term on the RHS of Eq. (F10) diverges logarithmically whenever $\Delta/\omega_c \to (n+1/2)$. On the other hand, it is evidently seen that when $\Delta = (n+1/2)\omega_c$ is satisfied, the two Landau levels $\pm E(n,k_z)$ become gapless at $k_z = 0$, and the size of the quantized magnetic orbit associated with the nth Landau level becomes exactly the same as the size of the nodal loop.

One may reproduce the above derivations for a NLSM with linear in-plane dispersions [see H_0^{lin} in Eq. (17)]. It turns out that for linear in-plane dispersions, the magnetic susceptibility is expressed as

$$\begin{aligned}\chi(B) =&\frac{eB}{2\pi^2\hbar}\left(\frac{ev_0^2}{\omega_c}\right)^2\sum_{n=0}^{\infty}\sqrt{n+\frac{1}{2}}\frac{\Delta}{\omega_c}\frac{2}{v}\ln l(n,\omega_c,\Delta)\\ &+\frac{e^2v_0^2}{\pi^2\hbar}\sum_{n=0}^{\infty}\sqrt{n+\frac{1}{2}}\left(\sqrt{n+\frac{1}{2}}-\frac{\Delta}{\omega_c}\right)\frac{2}{v}\ln l(n,\omega_c,\Delta)\\ &-\frac{eB}{2\pi^2\hbar}\left(\frac{ev_0^2}{\omega_c}\right)^2\sum_{n=0}^{\infty}\frac{2\Lambda\left(n+\frac{1}{2}\right)}{v\omega_c^2\sqrt{\left(\frac{\Delta}{\omega_c}-\sqrt{n+\frac{1}{2}}\right)^2+\Lambda^2}},\end{aligned} \tag{F12}$$

where

$$l(n,\omega_c,\Delta) = \frac{\sqrt{\left(\frac{\Delta}{\omega_c}-\sqrt{n+\frac{1}{2}}\right)^2+\Lambda^2}+\Lambda}{\left|\frac{\Delta}{\omega_c}-\sqrt{n+\frac{1}{2}}\right|}. \tag{F13}$$

The first term on the RHS of Eq. (F12) diverges logarithmically whenever $\Delta=\omega_c\sqrt{n+1/2}$. Again, such a condition is exactly the gap-closure condition of Landau levels; in the meanwhile, the nth magnetic orbit exactly overlaps with the nodal loop when $\Delta=\omega_c\sqrt{n+1/2}$.

[1] H. B. Nielsen and M. Ninomiya, Phys. Lett. B **130**, 389 (1983).
[2] A. A. Burkov and L. Balents, Phys. Rev. Lett. **107**, 127205 (2011).
[3] X. Wan, A. M. Turner, A. Vishwanath, and S. Y. Savrasov, Phys. Rev. B **83**, 205101 (2011).
[4] S. Murakami and S.-i. Kuga, Phys. Rev. B **78**, 165313 (2008).
[5] G. B. Halász and L. Balents, Phys. Rev. B **85**, 035103 (2012).
[6] A. M. Turner, A. Vishwanath, and C. O. Head, Topol. Insul. **6**, 293 (2013).
[7] P. Hosur and X. Qi, C. R. Phys. **14**, 857 (2013).
[8] J. Liu and D. Vanderbilt, Phys. Rev. B **90**, 155316 (2014).
[9] H. Weng, C. Fang, Z. Fang, B. A. Bernevig, and X. Dai, Phys. Rev. X **5**, 011029 (2015).
[10] B. Lv, H. Weng, B. Fu, X. Wang, H. Miao, J. Ma, P. Richard, X. Huang, L. Zhao, G. Chen *et al.*, Phys. Rev. X **5**, 031013 (2015).
[11] B. Q. Lv, N. Xu, H. M. Weng, J. Z. Ma, P. Richard, X. C. Huang, L. X. Zhao, G. F. Chen, C. E. Matt, F. Bisti *et al.*, Nat. Phys. **11**, 724 (2015).
[12] S.-M. Huang, S.-Y. Xu, I. Belopolski, C.-C. Lee, G. Chang, B. Wang, N. Alidoust, G. Bian, M. Neupane, C. Zhang *et al.*, Nat. Commun. **6**, 7373 (2015).
[13] A. A. Soluyanov, D. Gresch, Z. Wang, Q. Wu, M. Troyer, X. Dai, and B. A. Bernevig, Nature (London) **527**, 495 (2015).
[14] A. Liang, J. Huang, S. Nie, Y. Ding, Q. Gao, C. Hu, S. He, Y. Zhang, C. Wang, B. Shen *et al.*, arXiv:1604.01706.
[15] Z. Wang, Y. Sun, X.-Q. Chen, C. Franchini, G. Xu, H. Weng, X. Dai, and Z. Fang, Phys. Rev. B **85**, 195320 (2012).
[16] Z. Liu, B. Zhou, Y. Zhang, Z. Wang, H. Weng, D. Prabhakaran, S.-K. Mo, Z. Shen, Z. Fang, X. Dai *et al.*, Science **343**, 864 (2014).
[17] Z. Wang, H. Weng, Q. Wu, X. Dai, and Z. Fang, Phys. Rev. B **88**, 125427 (2013).
[18] Z. Liu, J. Jiang, B. Zhou, Z. Wang, Y. Zhang, H. Weng, D. Prabhakaran, S. Mo, H. Peng, P. Dudin *et al.*, Nat. Mater. **13**, 677 (2014).
[19] M. Z. Hasan and C. L. Kane, Rev. Mod. Phys. **82**, 3045 (2010).
[20] X.-L. Qi and S.-C. Zhang, Rev. Mod. Phys. **83**, 1057 (2011).
[21] T. H. Hsieh, H. Lin, J. Liu, W. Duan, A. Bansil, and L. Fu, Nat. Commun. **3**, 982 (2012).
[22] L. Fu and C. L. Kane, Phys. Rev. Lett. **100**, 096407 (2008).
[23] X.-L. Qi, T. L. Hughes, S. Raghu, and S.-C. Zhang, Phys. Rev. Lett. **102**, 187001 (2009).
[24] A. A. Burkov, M. D. Hook, and L. Balents, Phys. Rev. B **84**, 235126 (2011).
[25] T. Bzdušek, Q. Wu, A. Rüegg, M. Sigrist, and A. A. Soluyanov, Nature (London) **538**, 75 (2016).
[26] Y. Wu, L.-L. Wang, E. Mun, D. D. Johnson, D. Mou, L. Huang, Y. Lee, S. L. Budko, P. C. Canfield, and A. Kaminski, Nat. Phys. **12**, 667 (2016).
[27] Q.-F. Liang, J. Zhou, R. Yu, Z. Wang, and H. Weng, Phys. Rev. B **93**, 085427 (2016).
[28] T. T. Heikkilä and G. E. Volovik, JETP Lett. **93**, 59 (2011).
[29] H. Weng, Y. Liang, Q. Xu, R. Yu, Z. Fang, X. Dai, and Y. Kawazoe, Phys. Rev. B **92**, 045108 (2015).
[30] R. Yu, H. Weng, Z. Fang, X. Dai, and X. Hu, Phys. Rev. Lett. **115**, 036807 (2015).
[31] M. Neupane, I. Belopolski, M. M. Hosen, D. S. Sanchez, R. Sankar, M. Szlawska, S.-Y. Xu, K. Dimitri, N. Dhakal, P. Maldonado, P. M. Oppeneer, D. Kaczorowski, F. Chou, M. Z. Hasan, and T. Durakiewicz, Phys. Rev. B **93**, 201104 (2016).
[32] L. M. Schoop, M. N. Ali, C. Straßer, A. Topp, A. Varykhalov, D. Marchenko, V. Duppel, S. S. Parkin, B. V. Lotsch, and C. R. Ast, Nat. Commun. **7**, 11696 (2016).
[33] Y.-H. Chan, C.-K. Chiu, M. Y. Chou, and A. P. Schnyder, Phys. Rev. B **93**, 205132 (2016).
[34] G. Bian, T.-R. Chang, R. Sankar, S.-Y. Xu, H. Zheng, T. Neupert, C.-K. Chiu, S.-M. Huang, G. Chang, I. Belopolski *et al.*, Nat. Commun. **7**, 10556 (2016)
[35] J. Zhao, R. Yu, H. Weng, and Z. Fang, Phys. Rev. B **94**, 195104 (2016).
[36] M. Hirayama, R. Okugawa, T. Miyake, and S. Murakami, Nature Commun. **8**, 14022 (2017).
[37] H. Huang, J. Liu, D. Vanderbilt, and W. Duan, Phys. Rev. B **93**, 201114 (2016).
[38] J. Hu, Z. Tang, J. Liu, Y. Zhu, J. Wei, and Z. Mao, arXiv:1604.01567.
[39] J. Hu, Z. Tang, J. Liu, X. Liu, Y. Zhu, D. Graf, K. Myhro, S. Tran, C. N. Lau, J. Wei, and Z. Mao, Phys. Rev. Lett. **117**, 016602 (2016).
[40] Y.-Y. Lv, B.-B. Zhang, X. Li, S.-H. Yao, Y. B. Chen, J. Zhou, S.-T. Zhang, M.-H. Lu, and Y.-F. Chen, Appl. Phys. Lett. **108**, 244101 (2016).
[41] N. B. Kopnin, T. T. Heikkilä, and G. E. Volovik, Phys. Rev. B **83**, 220503 (2011).
[42] T. T. Heikkilä and G. E. Volovik, in *Basic Physics of Functionalized Graphite*, edited by P. Esquinazi (Springer International Publishing, Berlin, Germany, 2016), pp.123-134.
[43] N. B. Kopnin, M. Ijäs, A. Harju, and T. T. Heikkilä, Phys. Rev. B **87**, 140503 (2013).
[44] Y. A. Bychkov and E. Rashba, JETP Lett. **39**, 78 (1984).
[45] J. A. Hertz, Phys. Rev. B **14**, 1165 (1976).
[46] A. J. Millis, Phys. Rev. B **48**, 7183 (1993).
[47] W. P. Su, J. R. Schrieffer, and A. J. Heeger, Phys. Rev. Lett. **42**, 1698 (1979).
[48] W. P. Su, J. R. Schrieffer, and A. J. Heeger, Phys. Rev. B **22**, 2099 (1980).
[49] We consider the (001) surface throughout the paper.
[50] Even though the shape of the nodal loop looks perfectly nested when $t_1=t_2$, the Fermi surface is not nested due to the dispersion of the nodal energy from t_0.
[51] S. LaShell, B. A. McDougall, and E. Jensen, Phys. Rev. Lett. **77**, 3419 (1996).

[52] Y. M. Koroteev, G. Bihlmayer, J. E. Gayone, E. V. Chulkov, S. Blügel, P. M. Echenique, and P. Hofmann, Phys. Rev. Lett. **93**, 046403 (2004).

[53] O. Krupin, G. Bihlmayer, K. Starke, S. Gorovikov, J. E. Prieto, K. Döbrich, S. Blügel, and G. Kaindl, Phys. Rev. B **71**, 201403 (2005).

[54] J. Nitta, T. Akazaki, H. Takayanagi, and T. Enoki, Phys. Rev. Lett. **78**, 1335 (1997).

[55] A. Uehara, H. Shinaoka, and Y. Motome, Phys. Rev. B **92**, 195150 (2015).

[56] We note that the critical interaction strength (U_c) characterized by the divergence of RPA susceptibilities as shown in Fig. 4(b) are slightly inconsistent with the U_c shown in the Hartree-Fock phase diagram in Fig. 3(a). This is because our Hartree-Fock calculations are carried out at zero temperature, and in a slab geometry of 50 primitive cells, while the RPA susceptibilities are calculated for a 30-unit-cell slab with finite-temperature formalism (see Appendix B), and the temperature is set as $0.0125t_1$.

[57] P. Coleman, *Introduction to Many-body Physics* (Cambridge University Press, Cambridge, England, 2015).

[58] For example, in Ref. [73] Kauppila *et al.* has argued using Ginzburg-Landau theory that the amplitude fluctuations of (possible) superconducting order parameters at the surface of nodal-loop metals make significant contributions to the heat capacity around the critical temperature, such that the Ginzburg number becomes on the order of unity. It was further argued that such strong fluctuation effects would be preserved at lower temperatures.

[59] T. Moriya, *Spin Fluctuations in Itinerant Electron Magnetism* (Springer Science & Business Media, Berlin, Germany, 2012), Vol. 56.

[60] S.-S. Lee, Phys. Rev. B **80**, 165102 (2009).

[61] M. A. Metlitski and S. Sachdev, Phys. Rev. B **82**, 075127 (2010).

[62] D. F. Mross, J. McGreevy, H. Liu, and T. Senthil, Phys. Rev. B **82**, 045121 (2010).

[63] D. Kalkstein and P. Soven, Surf. Sci. **26**, 85 (1971).

[64] It worthwhile to note that the assumption $t_2 = t_3$ does not change the analytic behavior of the dynamical susceptibility. We make such an assumption simply for the sake of convenience, otherwise the expressions would be cumbersome.

[65] Our simulations stop at $q_\parallel = 0.05$ because when $q_\parallel \lesssim 0.05$ the in-plane $\mathbf{k}$ mesh density becomes comparable with $1/q_\parallel$.

[66] P. Delplace, D. Ullmo, and G. Montambaux, Phys. Rev. B **84**, 195452 (2011).

[67] H. K. Pal, F. Piéchon, J.-N. Fuchs, M. Goerbig, and G. Montambaux, Phys. Rev. B **94**, 125140 (2016).

[68] B. Roy, arXiv:1607.07867.

[69] B. Pamuk, J. Baima, F. Mauri, and M. Calandra, arXiv:1610.03445.

[70] T. T. Heikkilä and G. E. Volovik, New J. Phys. **17**, 093019 (2015)

[71] P. E. Blöchl, O. Jepsen, and O. K. Andersen, Phys. Rev. B **49**, 16223 (1994).

[72] M. Taherinejad, K. F. Garrity, and D. Vanderbilt, Phys. Rev. B **89**, 115102 (2014).

[73] V. J. Kauppila, T. Hyart, and T. T. Heikkilä, Phys. Rev. B **93**, 024505 (2016).